Available online at www.sciencedirect.com
ScienceDirect
Geochimica et Cosmochimica Acta 75 (2011) 5686–5705
Geochimica et Cosmochimica Acta
www.elsevier.com/locate/gca

Constraining atmospheric oxygen and seawater sulfate concentrations during Paleoproterozoic glaciation: In situ sulfur three-isotope microanalysis of pyrite from the Turee Creek Group, Western Australia

Kenneth H. Williford [a,*], Martin J. Van Kranendonk [b,c], Takayuki Ushikubo [a], Reinhard Kozdon [a], John W. Valley [a]

[a] NASA Astrobiology Institute, Astrobiology Research Consortium, WiscSIMS, Department of Geoscience, University of Wisconsin, 1215 W. Dayton St., Madison, WI 53706, USA
[b] Geological Survey of Western Australia, 100 Plain St., East Perth, WA 6004, Australia
[c] School of Earth and Environment, The University of Western Australia, 35 Stirling Hwy., Crawley, WA 6009, Australia

Received 22 December 2010; accepted in revised form 7 July 2011; available online 11 August 2011

Abstract

Previous efforts to constrain the timing of Paleoproterozoic atmospheric oxygenation have documented the disappearance of large, mass-independent sulfur isotope fractionation and an increase in mass-dependent sulfur isotope fractionation associated with multiple glaciations. At least one of these glacial events is preserved in diamictites of the ~2.4 Ga Meteorite Bore Member of the Kungarra Formation, Turee Creek Group, Western Australia. Outcrop exposures of this unit show the transition from the Boolgeeda Iron Formation of the upper Hamersley Group into clastic, glaciomarine sedimentary rocks of the Turee Creek Group. Here we report in situ multiple sulfur isotope and elemental abundance measurements of sedimentary pyrite at high spatial resolution, as well as the occurrence of detrital pyrite in the Meteorite Bore Member. The 15.3‰ range of $\Delta^{33}S$ in one sample containing detrital pyrite (−3.6‰ to 11.7‰) is larger than previously reported worldwide, and there is evidence for mass-independent sulfur isotope fractionation in authigenic pyrite throughout the section ($\Delta^{33}S$ from −0.8‰ to 1.0‰). The 90‰ range in $\delta^{34}S$ observed (−45.5‰ to 46.4‰) strongly suggests microbial sulfate reduction under non-sulfate limiting conditions, indicating significant oxidative weathering of sulfides on the continents. Multiple generations of pyrite are preserved, typically represented by primary cores with low $\delta^{34}S$ (<−20‰) overgrown by euhedral rims with higher $\delta^{34}S$ (4–7‰) and enrichments in As, Ni, and Co. The preservation of extremely sharp sulfur isotope gradients (30‰/<4 μm) implies limited sulfur diffusion and provides time and temperature constraints on the metamorphic history of the Meteorite Bore Member. Together, these results suggest that the Meteorite Bore Member was deposited during the final stages of the "Great Oxidation Event," when pO_2 first became sufficiently high to permit pervasive oxidative weathering of continental sulfides, yet remained low enough to permit the production and preservation of mass-independent sulfur isotope fractionation.

1. INTRODUCTION

The Archean–Proterozoic transition was a time of profound change in the Earth system. Available evidence supports the view that organisms capable of oxygenic photosynthesis evolved sometime before ~2.7 billion years (Ga) ago (Summons et al., 2006; Buick, 2008; Waldbauer et al., 2009), and the free oxygen that they produced slowly transformed the chemistry of the surface oceans until the reservoirs of reduced gases, hydrothermal fluids, and minerals were sufficiently oxidized to allow the buildup of oxygen in what had been an anoxic atmosphere (Catling and

* Corresponding author. Tel.: +1 912 344 5677.
E-mail address: kwilliford@geology.wisc.edu (K.H. Williford).

0016-7037/$ - see front matter © 2011 Elsevier Ltd. All rights reserved.
doi:10.1016/j.gca.2011.07.010

Claire, 2005). The final phase of this transition, occurring sometime before 2.32 billion years ago (Bekker et al., 2004), is known as the "Great Oxidation Event" (GOE) (Holland, 1994, 2002). A series of glaciations, at least one of which was apparently global in extent (Evans et al., 1997; Kirschvink et al., 2000), occurred in concert with the rise of atmospheric oxygen (Eyles, 1993).

The sulfur isotopic record in Archean and Paleoproterozoic sedimentary rocks places important constraints on the timing of atmospheric oxygenation. Laboratory culture experiments with microbial sulfate reducers have shown that sulfur isotope fractionation and sulfate reduction rate is inhibited at sulfate concentrations below 200 μM (Habicht et al., 2002). In light of these experiments, expansion in the range of sulfur isotope compositions ($\delta^{34}S$)[1] of sedimentary sulfides at ~2.4 Ga is evidence that seawater sulfate concentrations were below 200 μM prior to this time (Habicht et al., 2002; Bekker et al., 2004; Canfield and Farquhar, 2009). Rare observations of fractionations >10‰ between sedimentary sulfate and sulfide minerals older than ~2.7 Ga (Cameron and Hattori, 1987; Shen et al., 2001) suggest that sulfate concentrations may have temporarily exceeded the 200 μM threshold in restricted basins, but the prevailing view is that enhanced oxidative weathering of continental sulfides due to rising atmospheric oxygen was required to elevate sulfate concentrations in the global ocean (Cameron, 1982; Bekker et al., 2004; Canfield and Farquhar, 2009).

Analytical developments enabling precise and accurate measurement of the rarer stable isotopes of sulfur (^{33}S and ^{36}S) revealed anomalous sulfur isotope compositions preserved in Archean rocks (Farquhar et al., 2000), and subsequent photochemical modeling constrained the atmospheric oxygen concentration under which these compositions could be produced and preserved (Pavlov and Kasting, 2002). In most chemical systems with three or more isotopes of a given element, the degree of fractionation depends upon the mass differences of the isotopes in question, and "mass-independence" occurs where isotopic compositions deviate from the observed mass-dependent relations. In the case of sulfur, these relations are $\delta^{33}S \approx 0.515 \times \delta^{34}S$ and $\delta^{36}S \approx 1.90 \times \delta^{34}S$ (Hulston and Thode, 1965). The degree of mass-independent sulfur isotope fractionation (S-MIF) between ^{32}S, ^{33}S and ^{34}S is reported as $\Delta^{33}S$, defined in this study as the difference between measured $\delta^{33}S$ values and an exponential reference fractionation line as described by the following equation (Farquhar et al., 2007a,b):

$$\Delta^{33}S = \delta^{33}S - 1000 * ((1 + \delta^{34}S/1000)^{0.515} - 1) \quad (1)$$

Photodissociation of SO_2 by ultraviolet (UV) radiation in the absence of oxygen can produce S-MIF in laboratory experiments (Farquhar et al., 2001). However, photochemical models predict that the reactions thought to produce the large, positive S-MIF observed in the rock record ($\Delta^{33}S$ up to 12‰) would also produce large, mass-dependent fractionations ($\delta^{34}S > 100‰$) that exceed any observed in rocks (Lyons, 2009). Remaining theoretical hurdles notwithstanding, models indicate that large S-MIF could be neither produced nor preserved in sediments under an atmospheric O_2 concentration $>10^{-5}$ times the present atmospheric level (PAL) due to the absorption of the requisite UV wavelengths by ozone and the dilution of any signature in the oceanic sulfate reservoir (Pavlov and Kasting, 2002).

In the decade since the discovery of S-MIF in Archean and Paleoproterozoic sedimentary rocks, efforts have been made to characterize more completely the range of S-MIF and $\delta^{34}S$ in the rock record to further constrain the timing of the rise in atmospheric oxygen and seawater sulfate. In the pioneering work of Farquhar et al. (2000), a total range in $\Delta^{33}S$ of −1.3‰ to 2‰ was reported, with a decrease in S-MIF to less than 0.35 ‰ occurring sometime between 2.45 and 2.25 Ga. Prior to the present study, the minimum and maximum published values of $\Delta^{33}S$ were −2.49‰ (Ono et al., 2003) and 11.18‰ (Kaufman et al., 2007), respectively. The lack of S-MIF and the low $\delta^{34}S$ (−23.91‰ to −35.31‰) measured in the Rooihoogte and Timeball Hill Formations (Bekker et al., 2004; Cameron, 1982), which lie between two glacial diamictites in the Transvaal Basin of South Africa, suggest that atmospheric oxygen had increased significantly by 2.316 ± 0.007 Ga (Hannah et al., 2004). Multiple sulfur isotope measurements of carbonate associated sulfate and chromium reducible sulfide in carbonates from the Transvaal Supergroup demonstrate that the transition from mass-independent to mass dependent sulfur isotope fractionation occurs in the upper Duitschland Fm (which underlies the Timeball Hill Fm), ~700 m above glacial diamictites at the base of the unit (Guo et al., 2009). This transition is accompanied by a ~5‰ positive excursion in $\delta^{13}C$, suggesting a causative link between enhanced primary productivity, increased burial of organic carbon in marine sediments, and atmospheric oxygenation (Bekker et al., 2001; Guo et al., 2009). In the correlative, glaciogenic Huronian Supergroup of North America, a decrease in $\Delta^{33}S$ of sedimentary pyrite from a range of −0.07‰ to 0.88‰ in the Pecors Formation to a range of -0.20 ± 0.27‰ to 0.13 ± 0.22‰ in the Espanola Formation places the disappearance of S-MIF within the second of three glacial diamictites (Papineau et al., 2007).

Here we present in situ measurements of $\delta^{34}S$, $\Delta^{33}S$ and elemental concentrations in pyrite from outcrop samples that bound and include glacial diamictites of the ~2.4 Ga Meteorite Bore Member of the Kungarra Formation in the Turee Creek Group of the Hamersley Province of Western Australia. Careful analyses of sulfide grains were made in petrographic context, and as such provide information about the extent of mass-dependent and mass-independent sulfur isotope fractionation during the deposition of the Meteorite Bore Member, the presence and provenance of detrital pyrite in the samples, and intra-grain variability related to sulfide paragenesis. These results suggest that the Meteorite Bore Member was deposited during a transitional period when atmospheric oxygen was low enough to permit the production and preservation of S-MIF, yet high enough to permit the enhanced delivery of sulfate to the oceans as a result of continental oxidative weathering on the continents.

[1] $\delta^x S = \left(\frac{{}^xR_{sample}}{{}^xR_{VCDT}} - 1\right) \times 1000(‰)$ where ${}^xR = {}^xS/{}^{32}S$, and $x = 33$, 34 or 36. VCDT refers to Vienna Cañon Diablo Troilite.

1.1. Geologic setting

The Meteorite Bore Member diamictite was first recognized as glaciogenic due to the presence of striated and faceted boulders at the type locality in the Hardey Syncline (Trendall, 1976, 1981) and tentatively correlated with the Gowganda Formation of the Huronian Supergroup. Later work on localities in the Duck Creek Syncline and at Yeera Bluff, ~60 km along strike to the northwest, found more conclusive evidence for a glacial origin of the Meteorite Bore Member including bending, penetration, and disruption of fine-scale bedding at the bases of large clasts (suggesting vertical emplacement of ice rafted debris, or dropstones) as well as stratal onlap of clasts by overlying, fine-grained sedimentary rocks (Martin, 1999). Age constraints for the Meteorite Bore Member are provided by the overlying 2209 ± 15 Ma Cheela Springs Basalt (Martin et al., 1998) and the 2449 ± 3 Ma Woongarra Rhyolite below the Boolgeeda Iron Fm at the top of the Hamersley Group (Barley et al., 1997). A later study found that baddeleyites in a sill intruding the Meteorite Bore Member have a $^{207}Pb/^{206}Pb$ age of 2208 ± 15 Ma (Müller et al., 2005), and detrital zircons in the Meteorite Bore Member indicate a maximum age of deposition of ca. 2420 Ma (Takehara et al., 2010).

The Turee Creek Group has a total thickness of 3–4 km, shallowing upwards from banded iron formation (BIF) of the conformably underlying Hamersley Group, to clastic sedimentary rocks and stromatolitic carbonates higher in the Turee Creek Group preserved in synclinal keels along the southern margin of the Pilbara Craton (Blake and Barley, 1992; Martin, 1999). Metamorphism does not exceed prehnite–pumpellyite–epidote facies (Smith et al., 1982).

The primary locality discussed in this study is a section near Duck Creek to which we henceforth refer as "Boundary Ridge" (Fig. 1) and represents an exposure of a conformable contact between the Boolgeeda Iron Formation at the top of the Hamersley Group and the Kungarra Formation at the base of the Turee Creek Group (Fig. 2). On this basis it is being considered as a candidate for the Global Stratotype Section and Point (GSSP) for the Archean–Proterozoic boundary (Van Kranendonk, 2010).

The section has little deformation and a northeast dip of 20°. Lithostratigraphy is shown in Fig. 3 and described below. The Boolgeeda Iron Fm is exposed as a dark red, magnetite–hematite banded iron formation (BIF) weathering grey-black. A 15 cm "transitional chert" unit conformably overlies the Boolgeeda Iron Fm and comprises thin bands of BIF that grade into jaspilitic chert and then into layered grey and jaspilitic chert. This is conformably overlain by a green, pyritic mudstone with sparse dropstones that marks the base of the Turee Creek Group and clastic, glaciomarine deposition. This mudstone is overlain by three beds of coarse sandstone containing angular to subangular quartz clasts, locally abundant detrital pyrite, and outsize clasts of porphyritic rhyolite, carbonate, and a variety of other lithologies within a matrix of silt. The uppermost of these sandstones overlies diamictite with abundant carbonate clasts in a silty matrix and contains a thin (1 cm), continuous carbonate bed. A series of shale beds overlies the sandstone units, interrupted by a distinctive, Mn-rich (7.4 wt.% MnO) BIF (Van Kranendonk, 2010). Thin banded grey chert beds, jaspilitic chert, and BIF overlie the shales, with a siltstone unit at the top of the outcrop (Van Kranendonk, 2010). Two of the samples analyzed in this study come from a correlative section at Deepdale: sample 4 (194504), taken from the lowest exposure of the first glaciogenic unit in the Meteorite Bore Member, and sample 8 (194507), taken from the BIF unit that overlies the diamictites.

2. SAMPLES AND METHODS

2.1. Description of samples and standards

2.1.1. Samples

Eight samples from outcrop exposures of the uppermost Hamersley Group and lowermost Turee Creek Group at the Boundary Ridge and Deepdale localities were analyzed in this study and are briefly described below in ascending stratigraphic order (Fig. 3). Samples are numbered 1–8 in ascending stratigraphic order, and original sample number code and locality are indicated in parentheses in the following discussion. Sample 1 (190573, Boundary Ridge) was taken from 35 cm below the top of the Boolgeeda Iron Formation and exhibits sub-mm scale laminations of quartz and iron oxides with abundant, euhedral magnetite crystals and rare, euhedral pyrite 10–15 μm in size. Samples 2 and 3 (190580-2 and 190580-1, Boundary Ridge) are from the bottom and top of the transitional jaspilitic chert unit at the top of the Hamersley Group and contain abundant euhedral magnetite. Pyrite in these chert samples occurs as euhedral crystals between 1 and 100 μm in size. Sample 4 (194504, Deepdale) comes from the lowest exposure of the first glaciogenic unit, a fissile, green-grey mudstone with rhyolitic dropstones. Pyrite is abundant in this sample, occurring predominantly as disseminated, euhedral or subhedral crystals from 1 to 400 μm in size and rarely as grains with anhedral, globular margins (see below). Samples 5 and 6 (190583 and 190578, Boundary Ridge) are glaciogenic sandstones with abundant detrital quartz and pyrite ranging from 1 to 5 μm euhedral crystals, to euhedral or subhedral crystals 10–100 μm in size (or agglomerations thereof), to grains with rounded, pitted margins. Sample 7 (190575, Boundary Ridge) is a glacial shale with dropstones and abundant euhedral and subhedral pyrite grains ranging in diameter from 1 to 100 μm and concentrated in layers with 1–5 mm spacing. Sample 8 (194507, Deepdale) is a BIF with sub-mm scale laminations of quartz and magnetite, the latter occurring as euhedral crystals up to 300 μm in diameter. Only one grain of pyrite of sufficient size for analysis was identified in this sample, a euhedral crystal ~15 μm in diameter.

2.1.2. Standard

The Balmat pyrite standard UWPy-1 was used during SIMS analyses to calibrate isotope ratios and to monitor precision. This standard was embedded in the center of each sample mount. Preparation of this standard is described in detail by Kozdon et al. (2010), including chemical

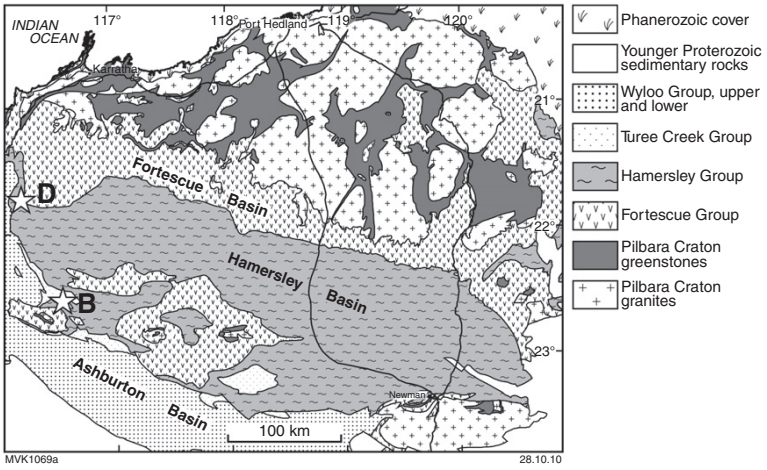

Fig. 1. Geologic map of the study area. Stars indicate sample localities (D: Deepdale; B: Boundary Ridge).

characterization by EPMA (wavelength dispersive spectroscopy) and $\delta^{34}S$ measurement by continuous flow mass spectrometry as $16.39 \pm 0.40‰$ (2 SD). This and other sulfur isotope compositions reported herein are given in standard delta notation $\delta^{34}S$ relative to Vienna Cañon Diablo Troilite (VCDT) with $(^{34}S/^{32}S)_{VCDT} = 0.044163$ (Ding et al., 2001). $\Delta^{33}S$ of UWPy-1 was measured at the University of Maryland as $-0.010 \pm 0.021‰$ (J. Farquhar, pers. comm.). Elemental abundances in grains of UWPy-1 standard are shown in the Electronic Annex (Table S1). Ni, Cu, Zn and As were all below detection limit with the single exception of a Zn content (0.04 wt.%) slightly above detection limit observed in the standard grain mounted together with sample 8. All standard grains except for that mounted with sample 4 contained trace, but measurable Co, up to a maximum of 0.07 wt.%.

2.2. Sample preparation

Offcuts from hand samples used to make thin sections (Fig. S8, Electronic Annex) were examined to select areas containing pyrite grains of sufficient size (>10 μm) and abundance for SIMS analysis. Two rectangular chips with a maximum linear dimension of approximately 1 cm were cut from each sample using a water-cooled diamond saw and arranged on double-stick tape on either side of a grain of UWPy-1 standard. Round epoxy mounts with a diameter of 25 mm and a thickness of 5 mm were prepared and polished with diamond paste until maximum surface relief was ~1 μm to minimize a topographic effect on isotope analyses (Kita et al., 2009). Surface topography was evaluated using a ZYGO™ white light profilometer at the Materials Science Center, University of Wisconsin–Madison. Mounts were cleaned by sonicating in deionized water (2×, 4 min), ethanol (30 s) and deionized water (3×, 1 min), drying first under high purity nitrogen and then in an evacuated oven overnight at 40 °C. Mounts were carbon coated to a thickness of 250 Å and degassed overnight at 10^{-9} Torr in the IMS-1280 sample airlock prior to SIMS analysis.

2.3. Morphological and elemental analysis

Individual pyrite grains were identified using optical and scanning electron microscopy (SEM, Hitachi S-3400) and energy dispersive X-ray spectroscopy (EDS). A 10 mm square at the center of each sample mount was mapped using a mosaic of backscattered electron (BSE) images taken at 140× (Figs. S9–S16, Electronic Annex). Individual pyrite grains were numbered on this map, and each grain was imaged in secondary electron (SE) and BSE modes at either 10 or 15 keV. All pyrite grains were classified according to their morphology (euhedral, subhedral, anhedral, or rounded), and Fig. 4 shows representative examples of each morphotype.

Electron probe microanalysis (EPMA) was performed on each grain using a CAMECA SX51 to confirm the phase and to quantify the concentrations of minor elements. The elements S, Fe, Co, Ni, Cu, Zn, As and Si were measured by wavelength spectrometry with a 20 keV accelerating potential and 60 nA electron beam current for 10 s each. Mn was also measured, counting for 20 s, although it was below detection limit (0.013 wt.%) in all cases. Calibration standards were as follows: Balmat pyrite (S), Elba Pyrite (Fe), Co metal (Co), Ni metal (Ni), Cu metal (Cu), Zn metal (Zn), Arsenopyrite Asp-200 (As), and Czamanske MnS (Mn). Analytical volume was approximately 3 μm in diameter. Probe for EPMA Software (Probe Software, Inc.) (Donovan, 2009) was used for data collection and reduction, and element maps were created using Surfer 9 (Scientific Software Group).

2.4. Sulfur isotope analysis

All sulfur isotope measurements reported in this study were conducted using the WiscSIMS CAMECA ims-1280 large radius multi-collector ion microprobe in the Department of Geoscience at the University of Wisconsin–Madison. Analytical procedures were similar to those previously reported for oxygen (Kita et al., 2009; Valley and Kita, 2009) and sulfur (Kozdon et al., 2010) isotope analyses from this laboratory, and further details are given below.

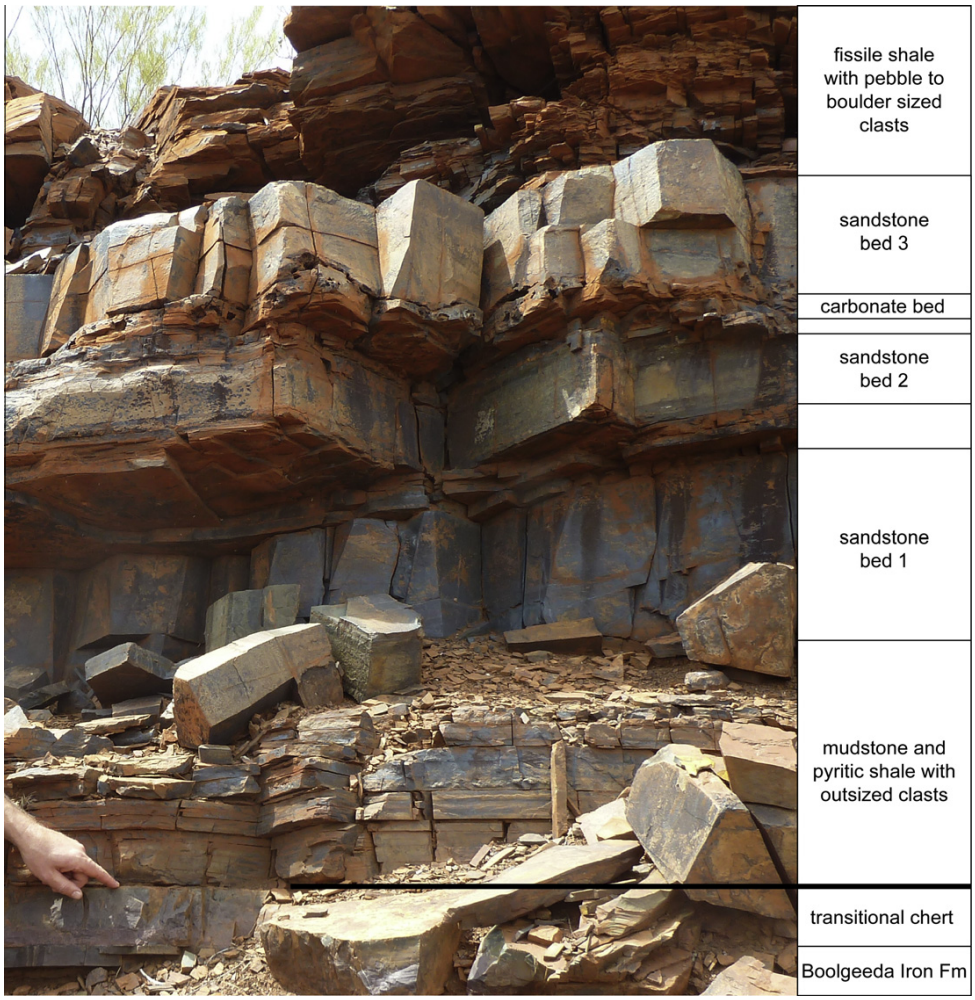

Fig. 2. Exposure of the Meteorite Bore member in outcrop at the Boundary Ridge locality (Fig. 1) with hand for scale. Finger is pointing at the contact between the "transitional chert" and the first siliciclastic unit, representing the onset of glaciomarine sedimentation. This also marks the conformable boundary between the uppermost Hamersley Group (Boolgeeda Iron Fm) and the lowermost Turee Creek Group. Lithologic descriptions are given in the stratigraphic column at right, shown in greater detail in Fig. 3.

2.4.1. Three sulfur isotope conditions

To perform in situ measurements of three isotopes of sulfur (^{32}S, ^{33}S, ^{34}S) with high spatial resolution and analytical precision, a primary $^{133}Cs^{+}$ ion beam with an intensity of ~1.5 nA and a total impact energy of 20 keV was focused to approximately 12 × 8 μm (~10 μm) at the surface of the sample. An electron gun oriented normal to the sample surface and carbon coating provided charge compensation. Secondary ions of three sulfur isotopes ($^{32}S^{-}$, $^{33}S^{-}$ and $^{34}S^{-}$) were collected simultaneously. A Faraday cup detector with a 10^{10} Ω resistor was used to measure secondary $^{32}S^{-}$ ions at the L′2 position, and Faraday cup detectors with 10^{11} Ω resistors were used to measure secondary $^{33}S^{-}$ and $^{34}S^{-}$ ions. Mass resolving power (M/ΔM, measured at 10% peak height) was set to ~5000. Analysis time consisted of 30 s for presputtering, 80 s for centering of secondary ions in the field aperture, and 80 s for analysis. To correct for interference caused by the overlap of the $^{32}SH^{-}$ and $^{33}S^{-}$ peaks, a measurement of the $^{32}SH^{-}$ peak intensity was made after each analysis by scanning the deflector that is located between the secondary mass filter magnet and the Faraday cup detectors (Heck et al., 2010). The ratio of $^{32}SH^{-}$ tail that overlaps the $^{33}S^{-}$ peak relative to the total $^{32}SH^{-}$ peak was determined to be 1.11×10^{-5} in the same session, and this was multiplied by the ratio of the two measured count rates to determine a correction factor. Correction for $^{32}SH^{-}$ contribution to the $^{33}S^{-}$ peak was negligible (0.0108‰ at most and 0.00136‰ on average) relative to the analytical reproducibility (typically ±0.09‰, 2 SD in $\Delta^{33}S$). Total analysis time, including $^{32}SH^{-}$ correction, was approximately 5 min.

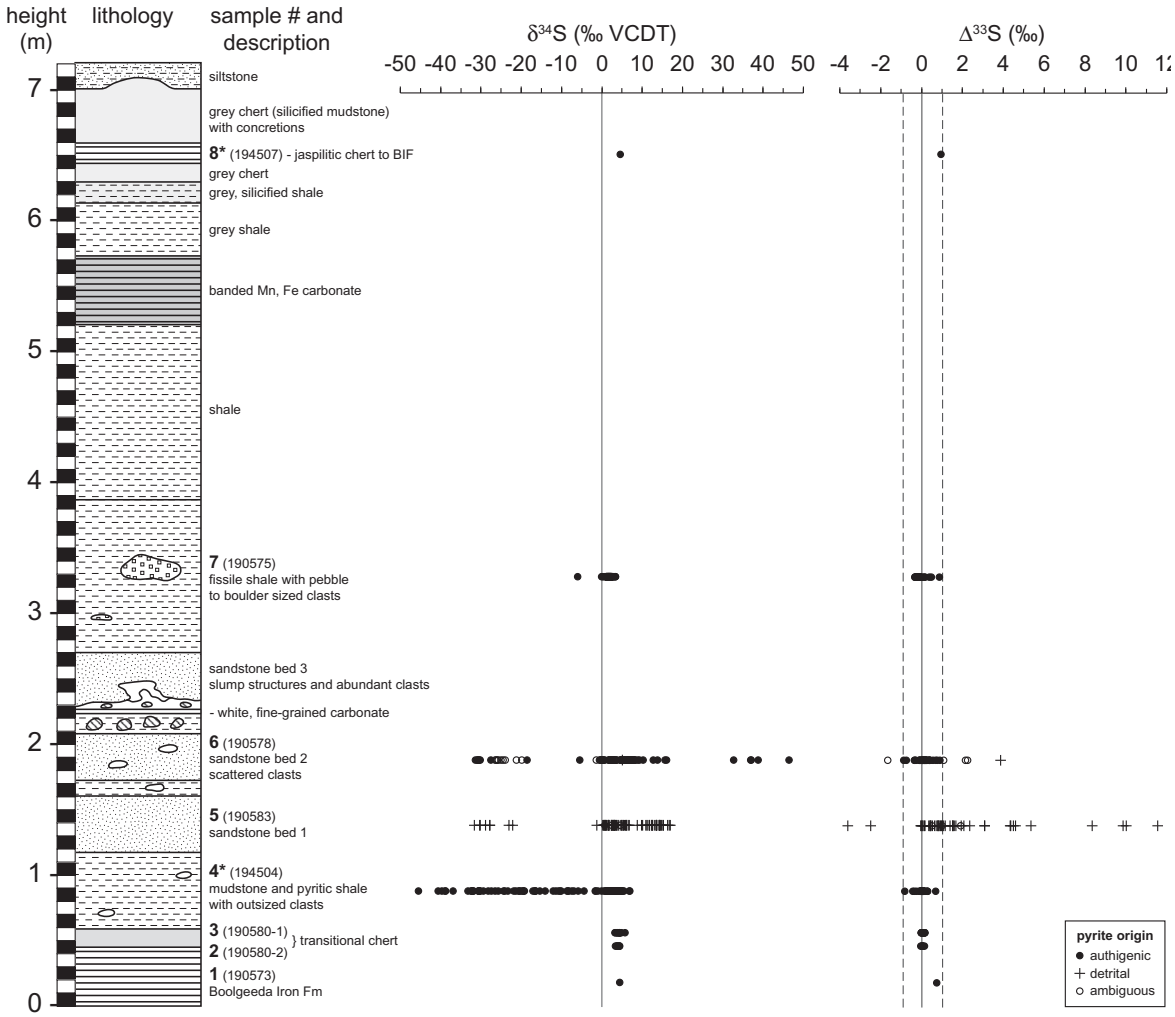

Fig. 3. Stratigraphy and sulfur isotope composition of pyrites from the Meteorite Bore Member of the Kungarra Formation (Turee Creek Group), Western Australia. All sulfur isotope analyses were made in situ at WiscSIMS. The top of the transitional chert bed at 0.6 m in the section represents the contact between the uppermost Hamersley and the lowermost Turee Creek Groups as well as the base of the Meteorite Bore Member. Analytical uncertainty (±2 SD) is smaller than data points. Dashed lines indicate the range of $\Delta^{33}S$ measured in unambiguously authigenic pyrite (−0.83‰ to 0.96 ± 0.09‰), and crosses indicate pyrite of detrital or ambiguous origin.

2.4.2. Two sulfur isotope conditions

In order to further evaluate sulfur isotopic heterogeneity within single grains, measurements were made using a $^{133}Cs^{+}$ primary ion beam with an intensity of 30 pA, which was focused to approximately 3 × 2 μm at the surface of the sample. The secondary $^{34}S^{-}$ and $^{32}S^{-}$ ions were simultaneously collected by two Faraday cup detectors, with a secondary ion intensity of ~2.5 × 10^{7} for $^{32}S^{-}$. An electron flood gun in combination with a carbon coat was used for charge compensation. Mass resolving power, measured at 10% peak height, was set to 2200. The total analytical time per spot was about 5 min including presputtering (2 min), automatic centering of the secondary ion image in the field aperture (90 s), and analysis (80 s). The baseline noise level of the Faraday cups was monitored during presputtering.

2.5. Sulfur isotope data reduction

Isotopic analyses by SIMS are affected by a systematic bias sometimes called "instrumental mass fractionation" (henceforth referred to as "bias") and related to sputtering processes as well as differences in the efficiency of ionization, transmission, and detection of individual isotopes. To correct for these effects, four analyses of the UWPy-1 standard grain, located at the center of each sample mount, were made before and after each set of 8–12 unknown sample analyses. For $\delta^{34}S$, a correction factor was determined

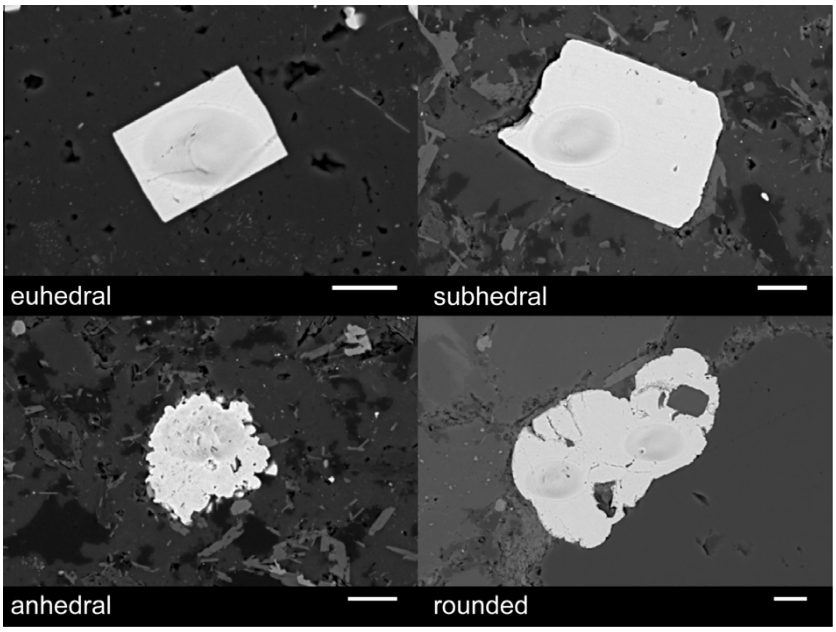

Fig. 4. Representative examples of pyrite grain morphotypes from the Meteorite Bore Member of the Turee Creek Group, Western Australia. Ion probe pits from the March 23–27, 2010 analytical session at WiscSIMS are visible. Scale bars are 10 μm.

for each of these brackets by comparing the average measured value of the standard with its known value ($16.39 \pm 0.40‰$ VCDT, 2 SD).

The calculation of $\Delta^{33}S$ follows procedures described for $\Delta^{17}O$ by Kita et al. (2010). First, raw $\delta^{34}S$ and $\delta^{33}S$ values (after applying the $^{32}SH^-$ correction described above, but uncorrected for instrumental bias) were used to calculate raw $\Delta^{33}S$ as shown in Eq. (1). We assumed that the $\Delta^{33}S$ value of the Mesoproterozoic UWPy-1 standard is 0‰, and applied a correction factor to sample analyses based upon the average raw $\Delta^{33}S$ of the bracketing standards. The absence of S-MIF in UWPy-1 is supported by analyses of Ruttan pyrite described under Results and by analyses of UWPy-1 at the University of Maryland ($\Delta^{33}S = -0.010 \pm 0.021‰$ (J. Farquhar, pers. comm.). The average raw $\Delta^{33}S$ for all UWPy-1 analyses in the study was $0.09 \pm 0.13‰$ (2 SD). We recalculated $\delta^{33}S$ CDT for unknown sample analyses by solving Eq. (1) for $\delta^{33}S$, using the $\delta^{34}S$ CDT and the corrected $\Delta^{33}S$ values. For unknown sample analyses, the reported uncertainty in $\delta^{34}S$ and $\Delta^{33}S$ is two standard deviations of the eight bracketing standard measurements, and the reported uncertainty in $\delta^{33}S$ is a quadratic propagation of these two values.

3. RESULTS

Elemental abundance data for all standard and sample grains are reported in the Electronic Annex (Table S1), and data for samples are summarized below. Backscattered electron images of all analyzed grains, thin section photomicrographs, and backscattered electron mosaic images of analytical regions for all samples are shown in the Electronic Annex (Figs. S5–S16). Summary sulfur isotope data for standards are discussed below and shown in Table 1. Data for all individual analyses of standards and samples are reported in the Electronic Annex (Tables S1–S4) and shown in Fig. 3.

3.1. Standards and analytical precision

EPMA of UWPy-1 grains used in this study confirms the results of Kozdon et al. (2010), demonstrating that Ni, Cu, Zn, As and Si are below detection limit, and shows Co contents (0.05 wt.%) only slightly above detection limit for that element (0.037 wt.%).

For 144 analyses of UWPy-1 [$\delta^{34}S = 16.39 \pm 0.4‰$ VCDT, 2 SD (Kozdon et al., 2010)] during the sulfur three-isotope, 10 μm spot session, average external precision (spot-to-spot reproducibility) for all brackets was 0.20‰ for $\delta^{34}S$, 0.15‰ for $\delta^{33}S$ and 0.09‰ for $\Delta^{33}S$ ($n = 30$ brackets, 2 SD). Four analyses of four different grains of Ruttan pyrite [~1.88 Ga (Barrie et al., 2005); $\delta^{34}S = 1.2 \pm 0.1‰$ (Crowe and Vaughan, 1996)] had a variability in $\delta^{34}S$ of 0.13‰ at 2 SD. Average raw $\Delta^{33}S$ for four Ruttan pyrite analyses was 0.05‰, and average raw $\Delta^{33}S$ for all 144 UWPy-1 analyses was 0.09‰. This supports the conclusion that there is no detectable inherited S-MIF in the Mesoproterozoic UWPy-1 standard. For 80 analyses of UWPy-1 during the first sulfur two isotope, 3 μm spot session, average spot-to-spot reproducibility for all brackets was 0.72‰ for $\delta^{34}S$ ($n = 15$, 2 SD). For 36 analyses of UWPy-1 during the second sulfur two isotope, 3 μm spot session, average spot-to-spot reproducibility for all brackets was 0.82‰ for $\delta^{34}S$ ($n = 7$, 2 SD).

Table 1
Summary of uncorrected sulfur three-isotope data for standards analyzed at WiscSIMS during the March 23–27, 2010 session using a 10 μm spot. Delta values are normalized relative to VCDT value reported by Ding et al. (2001). Each sample number represents a different 25 mm mount. Data shown are averages and 2 standard deviations of individual spot-analyses of the UWPy-1 standard grain mounted together with each sample. Data for WI-STD 50 and WI-STD 45 represent analyses of separate grains of either Balmat (UWPy-1) or Ruttan pyrite in two standard mounts. Data for individual analyses are shown in the Electronic Annex.

Sample	*n*	$\delta^{34}S_{RAWavg}$ (‰)	±2 SD	$\delta^{33}S_{RAWavg}$ (‰)	±2 SD	$\Delta^{33}S_{RAWavg}$ (‰)	±2 SD
WI-STD50 UWPy-1	20	19.03	0.37	9.74	0.22	−0.01	0.14
WI-STD45 UWPy-1	8	18.97	0.59	9.76	0.32	0.04	0.11
WI-STD45 Ruttan	4	4.53	0.13	2.38	0.06	0.05	0.05
8 (194507 UWPy-1)	8	19.05	0.19	9.83	0.09	0.07	0.07
7 (190575 UWPy-1)	20	19.19	0.20	9.93	0.13	0.10	0.10
6 (190578 UWPy-1)	24	19.05	0.25	9.86	0.18	0.10	0.09
5 (190583 UWPy-1)	36	19.28	0.33	9.99	0.23	0.10	0.10
4 (194504 UWPy-1)	38	19.10	0.56	9.90	0.36	0.11	0.12
3 (190580-1 UWPy-1)	12	18.89	0.46	9.79	0.27	0.10	0.07
2 (190580-2 UWPy-1)	8	19.01	0.15	9.84	0.16	0.10	0.12
1 (190573 UWPy-1)	8	19.27	0.13	10.00	0.15	0.12	0.14

3.2. Sample analyses

A summary of sulfur isotope data is shown in Table 2, and in relation to stratigraphic order in Fig. 3. Average minor element concentrations for sample grains are low: 0.16 wt.% (Co), 0.15 wt.% (Ni), 0.08 wt.% (Cu), 0.04 wt.% (Zn), and 0.37 wt.% (As). Enrichments in As of up to 2.5 wt.% were observed in several grains. We have not evaluated, and thus cannot rule out the possibility of a small matrix effect on analyses of $\delta^{34}S$ related to As concentration, which is as high as 2.5 wt.% in one domain of one crystal, but we expect that any such effect would be at the 0.*x*‰ level for $\delta^{34}S$. A small difference in bias should not affect $\Delta^{33}S$ and would not affect the interpretations presented here.

3.2.1. Sample 1 (190573)

Pyrite occurs in this sample mainly as finely disseminated, submicrometer grains too small for high-accuracy in situ analysis using the techniques applied in this study. However, one ~15 μm, euhedral pyrite crystal, associated with fine-grained quartz and ~100 μm magnetite crystals, was identified and selected for analysis. The grain has a $\delta^{34}S$ of 4.4‰ and a $\Delta^{33}S$ of 0.73‰, and Co is the only minor element detected (0.1 wt.%).

3.2.2. Samples 2 and 3 (190580-2 and 190580-1)

Pyrite grains in these "transitional chert" samples were either sub- or euhedral, occurring as finely disseminated, smaller crystals <1 to a few μm in size, or larger crystals up to ~200 μm concentrated with iron oxides in bedding-parallel bands. Minor elements were detected in 14 of 20 grains, with compositions of up to 0.29 wt.% in Co, 0.36 wt.% in Ni and 0.71 wt.% in As. Arsenic was the most common minor element present, averaging 0.30% among grains in which it was detected. The range of $\delta^{34}S$ is small, from 3.2‰ to 5.8‰ with an average of 4.1‰, and 6 of 20 grains have $\Delta^{33}S > 0.1$‰ with a maximum of 0.18‰.

3.2.3. Sample 4 (194504)

This mudstone sample contains dropstones and represents the lowest Proterozoic glacial deposit in the section. Pyrite is distributed evenly throughout the sample as sub- and euhedral crystals ranging in size from <1 to >300 μm. A total of 103 isotopic measurements were made in this sample, distributed among 34 different grains of pyrite. Measurements using three-isotope conditions were made of 32 individual grains, followed by two-isotope analyses of 7 of these grains. The sample was then repolished to remove analytical pits, and 2 of the original grains were reanalyzed along with 2 additional grains that had not been previously

Table 2
Summary of in situ sulfur isotope data for Meteorite Bore Member pyrites. A total of 465 analyses were made from 149 grains at WiscSIMS. Delta values are normalized relative to VCDT value reported by Ding et al. (2001). The total number of grains analyzed in each sample is shown in second column. Data for $\delta^{34}S$ (VCDT) come from 3 separate analytical sessions (March 23–27, June 8–10, and August 13–14, 2010), the first using a 10 μm spot and the latter two using a 3 μm spot. Data for $\delta^{33}S$ and $\Delta^{33}S$ come from the 10 μm spot analytical session only. Data for individual analyses are shown in the Electronic Annex.

Sample	*n*	$\delta^{34}S_{min}$ (‰ VCDT)	$\delta^{34}S_{max}$ (‰ VCDT)	$\delta^{33}S_{min}$ (‰ VCDT)	$\delta^{33}S_{max}$ (‰ VCDT)	$\Delta^{33}S_{min}$ (‰)	$\Delta^{33}S_{max}$ (‰)
8	1	4.49	4.49	3.28	3.28	0.96	0.96
7	30	−5.95	3.39	−3.40	2.08	−0.34	0.87
6	27	−31.42	46.43	−15.96	19.31	−1.64	3.90
5	36	−31.64	17.04	−18.87	18.43	−3.57	11.73
4	34	−45.46	6.87	−19.28	3.61	−0.83	0.68
3	13	3.18	5.76	1.71	3.01	−0.03	0.18
2	7	3.33	4.40	1.79	2.40	−0.03	0.14
1	1	4.44	4.44	3.02	3.02	0.73	0.73

analyzed. All grains have measurable concentrations of minor elements. Compositions of up to 0.79 wt.% in Co, 0.32 wt.% in Ni, and 1.04 wt.% in As were measured. Multiple generations of pyrite and distinct overgrowths are clearly observed in 6 (of ~70) grains, initially as differences in gray-scale in BSE images. The rims of these grains appear brighter in BSE and have subhedral margins, minor element enrichments, and a relatively homogeneous $\delta^{34}S$ of approximately 4‰. Cores appear darker in BSE and have irregular margins, low or undetected As, Ni, and Co, and more heterogeneous $\delta^{34}S$ from −19‰ to −46‰, with an average of −30‰ (Fig. 5). Isotopic compositions in this sample range from −45.5‰ to 6.9‰ in $\delta^{34}S$ and from −0.8‰ to 0.7‰ in $\Delta^{33}S$.

3.2.4. Sample 5 (190583)

This glacial sandstone contains abundant detrital pyrite that occurs as grains with rounded margins and sometimes pitted surfaces (Fig. 6). In some cases, rounded, pitted grains are associated with euhedral pyrite and arsenopyrite overgrowths, as well as carbonaceous material (Fig. 7). Pyrite is evenly distributed among sand-sized detrital quartz grains and larger (>2 mm) porphyritic clasts. Of the grains selected for analysis, one is euhedral, five are subhedral, three are anhedral, and 27 are rounded. In total, 91 sulfur isotope analyses were made. Concentrations of up to 0.59 wt.% in Co, 0.55 wt.% in Ni, and 1.45 wt.% in As were measured, and the highest As content occurs in a subhedral grain (Table S1, Electronic Annex). This sample shows a much wider range in $\Delta^{33}S$ than any other sample in the study, from −3.57‰ to 11.73‰, and $\delta^{34}S$ varies from −31.6‰ to 17.0‰.

3.2.5. Sample 6 (190578)

Sample 6 is a moderately sorted glacial sandstone with abundant detrital quartz grains up to 1 mm in size. The evenly distributed pyrite in this sample is almost uniformly euhedral or subhedral. Out of 27 individual grains, only one was interpreted to be detrital on the basis of its rounded margin (grain 19). The pattern of distribution and association with rounded, detrital quartz suggests that a detrital origin is likely for other pyrite grains in this sample. Of 26 grains classified as either authigenic or ambiguous in origin (i.e. authigenic vs. detrital), 41 analyses of $\Delta^{33}S$ range from −1.6‰ to 2.3‰, and 112 analyses of $\delta^{34}S$ range from −31.4‰ to 46.4‰. Multiple generations of pyrite were observed in five (of ~50) grains, two of which are shown in Fig. 5c and d. Four grains show a similar pattern to zoned grains in sample 4, although with different characteristic sulfur isotope compositions: cores have an average $\delta^{34}S$ of −27.4‰, while rims have an average $\delta^{34}S$ of 6.6‰ (Fig. 8). Grain 3 shows two relatively high $\delta^{34}S$ generations of pyrite, with an average $\delta^{34}S$ of 7.0‰ in the core and 2.5‰ in the rim. A map of elemental distributions in grain 49 shows Co (0.6 wt.%), Ni (0.9 wt.%) and As (2.5 wt.%) concentrated in the rim, as well as a minor Cu content concentrated in the core (Fig. 9).

3.2.6. Sample 7 (190575)

Pyrite grains in this glacial shale are uniformly euhedral or subhedral, occur in mm-scale, bedding parallel bands, and exhibit less variability in sulfur isotope and minor element composition than stratigraphically lower, coarser grained siliciclastic units. For the 30 individual grains

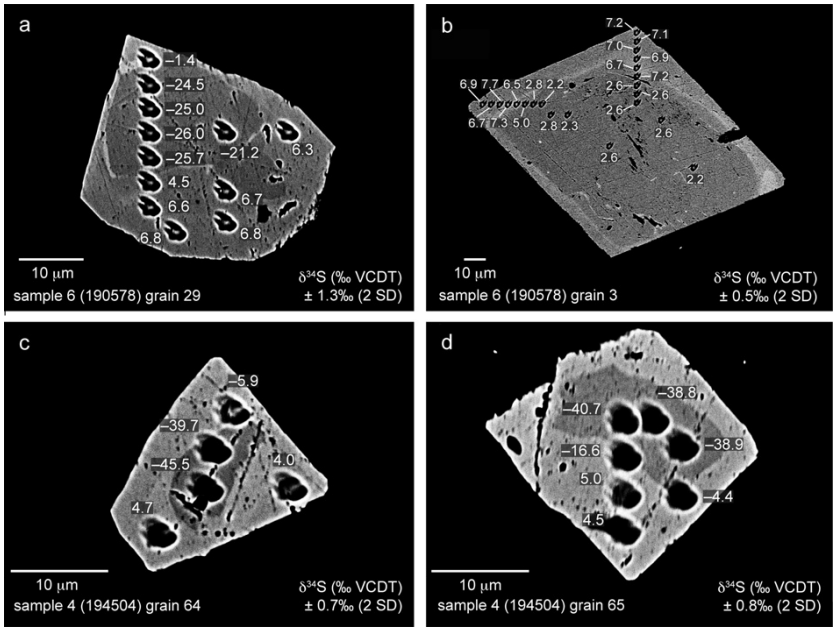

Fig. 5. (a–d) Backscattered electron images of pyrite grains showing analytical pits from WiscSIMS and measured $\delta^{34}S$ values from the Meteorite Bore Member of the Turee Creek Group, Western Australia. Darker cores and brighter rims are isotopically distinct. Rims have $\delta^{34}S$ consistent with a hydrothermal origin, whereas cores in a, c and d have low $\delta^{34}S$ consistent with an origin from microbial sulfate reduction. Analytical pits that straddle core–rim boundaries have intermediate $\delta^{34}S$ reflecting mixing of distinct zones.

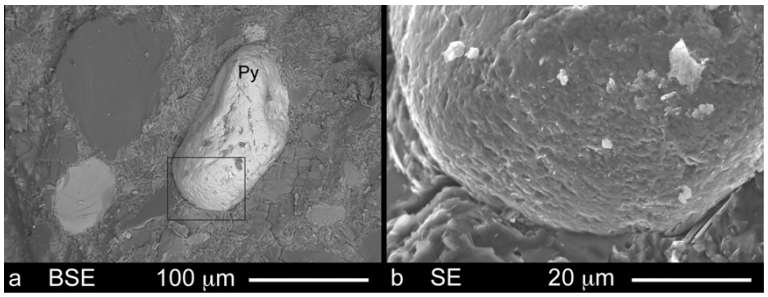

Fig. 6. Backscattered electron image of detrital pyrite grain in sample 5 (a). Square indicates area of enlargement in a secondary electron image (b) showing surface pitting.

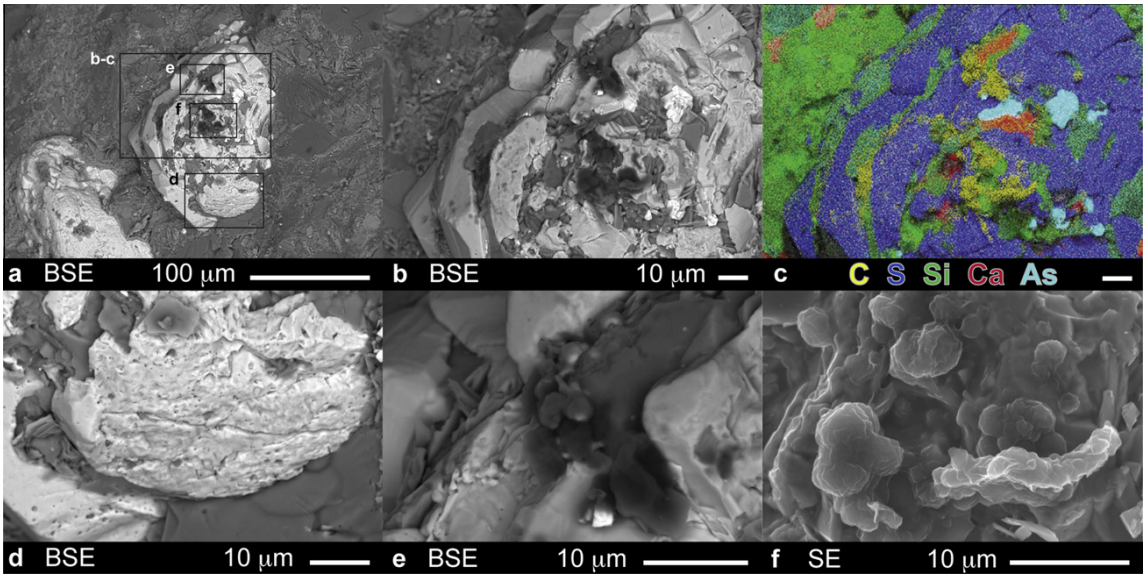

Fig. 7. Scanning electron micrographs of a rounded, detrital pyrite grain with euhedral, secondary pyrite overgrowth in a broken surface of sample 5. A backscattered electron (BSE) overview image indicating areas of enlargement is shown in (a). An enlargement of the upper surface of the grain is shown in BSE in (b), and (c) shows a map of elemental abundances in the same field of view measured by energy dispersive spectroscopy. Carbonaceous structures appear as a diffuse dark gray in BSE (b) and are indicated in yellow in (c). Small arsenopyrite grains in overgrowth appear as light blue (As), and calcium carbonate appears as red/yellow overgrowths in (c). A platy mineral with EDS spectrum consistent with potassium feldspar appears as a lighter gray in BSE and is shown in green in (c). This material appears to occur under the original, rounded and pitted surface of the detrital grain and between this surface and the euhedral overgrowth as seen in (d). An intimate association between carbonaceous and platy material is seen in (e) suggesting that the carbonaceous material is associated with the original grain and predates euhedral overgrowths. An enlargement of carbonaceous material is shown as a secondary electron image in (f). Scale bars are 100 μm in (a) and 10 μm in (b–f).

analyzed in this sample, the range in $\delta^{34}S$ is from −6.0‰ to 2.6‰, and the range in $\Delta^{33}S$ is from −0.3‰ to 0.9‰. Minor elements are below detection limits in 16 of 30 grains, and maximum concentrations of 0.07 wt.% for Co, 0.11 wt.% for Ni and 0.31 wt.% for As were measured among the remaining grains.

3.2.7. Sample 8 (194507)

This sample from the uppermost BIF in this study contains only one pyrite grain of sufficient size for sulfur three-isotope analysis, a ~15 μm, euhedral crystal within a chert band surrounded by iron oxides. This grain has $\delta^{34}S$ of 4.5‰, $\Delta^{33}S$ of 0.96‰, and low, but measurable concentrations of Co (0.05 wt.%) and Zn (0.04 wt.%).

4. DISCUSSION

4.1. Source of sulfur in Meteorite Bore pyrites

In this study we have identified three different types of pyrite. Authigenetic pyrite formed in place, as a result of early diagenetic sulfate reduction. Detrital pyrite was

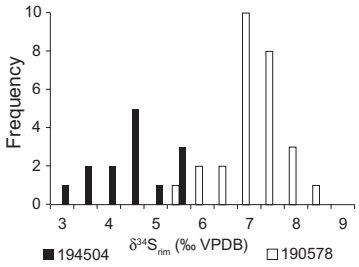

Fig. 8. Frequency histograms showing distinct $\delta^{34}S$ values of pyrite rims as measured with 3 μm spots in three grains (24, 64, 65) from sample 4 and three grains (3, 15, 29) from sample 6 where clear distinctions between cores and rims were observed in backscattered electron (BSE) images. Average analytical precision for these small spot analyses was 0.76‰ (2 SD).

weathered out of older rocks or sediments located at some significant distance from the site of deposition, and then transported, abraded, and deposited as part of the sedimentary succession. Secondary pyrite formed as a result of fluid interactions during metamorphism or late diagenesis (including hydrothermal alteration).

A potentially confounding factor in the analysis of sedimentary sulfides deposited before and during the GOE is the contribution of detrital pyrite, as the original isotopic composition of this material was set by conditions that existed in an unknown environment at an unknown time *before* the deposition of the host sediment. Previous studies have sought to distinguish a detrital component in Paleoproterozoic glaciogenic rocks with some difficulty (Papineau et al., 2005, 2007). Because detrital pyrite could have originally formed from any of a number of possible earlier mechanisms (i.e. igneous, metamorphic, hydrothermal, diagenetic, abiotic or biotic), identification based on isotopic or elemental composition alone could be ambiguous. Morphological clues can be obscured as well, if grain margins that were rounded during transport are later masked by euhedral overgrowths, although compositional differences between successive generations of pyrite in a single grain can sometimes be observed using BSE images. We evaluated each grain that we analyzed using criteria including morphology (grain margins as well as compositional zoning revealed in BSE images), minor element composition, and petrographic relations with surrounding grains in order to determine whether or not the grain was detrital.

4.1.1. Detrital pyrite

Clear evidence for detrital pyrite in the Meteorite Bore Member comes from the rounded, pitted surfaces of grains as revealed by SEM images, for example, of the broken surface of sample 5 (Figs. 6 and 7). Fig. 7 shows a pyrite grain with a rounded, pitted surface that is partially covered by euhedral pyrite and arsenopyrite overgrowths and by globular carbonaceous material that is concentrated in surficial cavities and at the interface between rounded and euhedral surfaces. The carbonaceous material is intimately associated with a platy mineral that has an EDS spectrum consistent with K-feldspar and appears to underlie euhedral overgrowths in SEM images (Fig. 7d). We interpret this grain to represent detrital pyrite that was associated with organic matter before, during, or immediately after deposition and later overgrown by secondary sulfides.

A positive correlation between $\delta^{34}S$ and $\Delta^{33}S$ is evident in detrital pyrite from samples 5 and 6 (Fig. 10), similar to that observed in the ~2.7 Ga Jeerinah Fm and ~2.5 Ga Mount McRae Shale in Western Australia (Ono et al., 2003) as well as the ~2.5 Ga Klein Naute Fm in South Africa (Ono et al., 2009). Pyrite with positive $\delta^{34}S$ and large, positive $\Delta^{33}S$ likely received its sulfur from atmospheric S_8, whereas pyrite with negative $\Delta^{33}S$ and large,

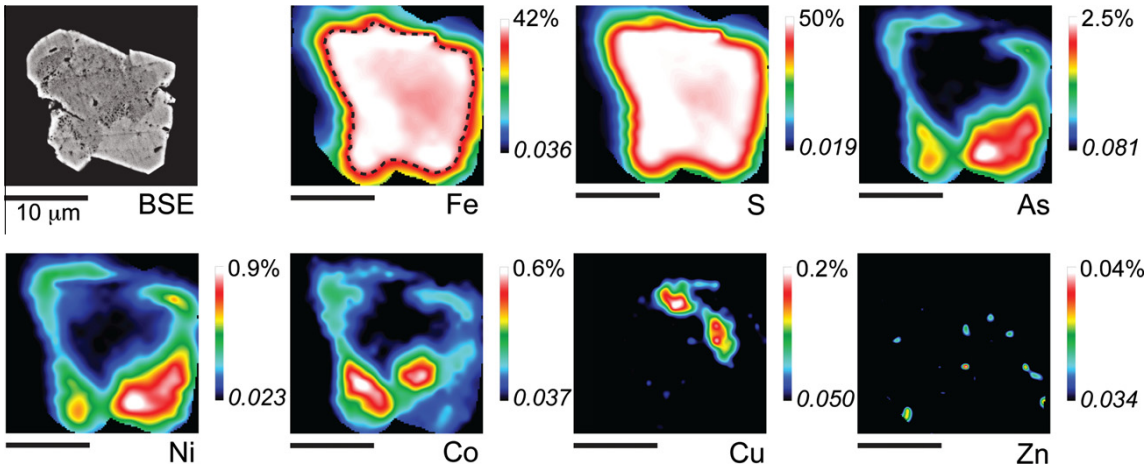

Fig. 9. Elemental distributions in pyrite grain 49 from sample 6. Maps are constructed from 453 individual electron microprobe analyses distributed with 1 μm spacing over the surface of the grain. Numbers in italics indicate detection limits for individual elements. Distinct core and rim morphology appears as differences in grayscale in the backscattered electron (BSE) image in the top left panel. As, Ni, and Co are enriched in the rim, whereas Cu is concentrated in the core. Dashed line on Fe map shows approximate grain boundary. Apparent zoning in Fe and S near grain boundary is an edge effect related to secondary fluorescence (Fournelle et al., 2005). Scale bars are 10 μm.

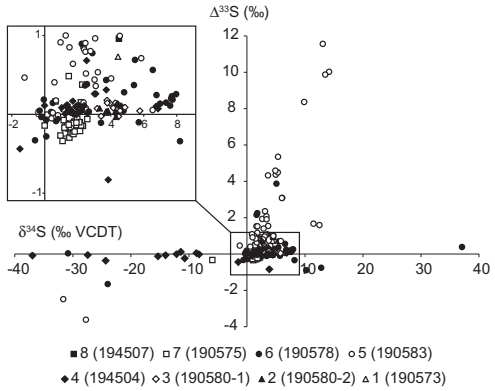

Fig. 10. Multiple sulfur isotope data for pyrite measured at WiscSIMS in situ from eight samples from the Meteorite Bore Member. Samples 5 and 6 contain a pyrite component of detrital or ambiguous origin (including all pyrite grains with $1‰ < \Delta^{33}S < -1‰$). The region around the origin is enlarged for clarity. Detrital pyrite in samples 5 and 6 demonstrates positively correlated $\delta^{34}S$ and $\Delta^{33}S$ (highlighted in gray) similar to that reported in earlier studies of late Archean rocks from the Hamersley and Griqualand West Basins (Ono et al., 2003, 2009).

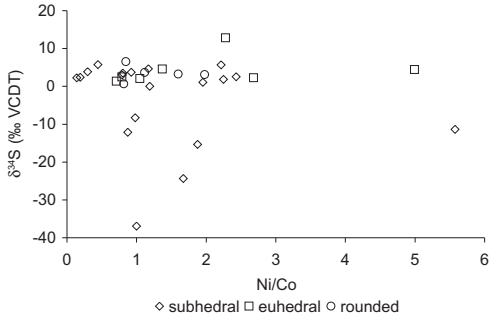

Fig. 11. Sulfur isotope composition vs. Ni/Co in Meteorite Bore Member pyrites with both Ni and Co present above minimum detection limits. Grains are grouped by morphology, and rounded grains are classified as detrital. Grains with $\delta^{34}S$ indicative of microbial sulfate reduction have Ni/Co > 0.8.

negative $\delta^{34}S$ likely resulted from the bacterial reduction of seawater sulfate that acquired its S-MIF signature as atmospheric H_2SO_4 (Ono et al., 2003).

4.1.2. Pyrite paragenesis

All samples from clastic units in the Meteorite Bore Member studied herein (samples 4–7) show evidence for multiple generations of sulfide with distinct sources of sulfur. Pyrite overgrowths were initially apparent in BSE images showing grains with darker cores and brighter rims, and chemical differences were later confirmed with small spot sulfur isotope analysis (Fig. 5) and EPMA (Fig. 9). Often, the darker cores of grains have $\delta^{34}S < -20‰$, suggesting that they formed as a result of microbial sulfate reduction (Machel et al., 1995). The rims have significantly higher $\delta^{34}S$ ($\geqslant 4‰$), consistent with either quantitative reduction of sulfate by microorganisms or deposition from a late diagenetic or metamorphic fluid. In some cases, cores with $\delta^{34}S > 0‰$ are overgrown by pyrite rims with a distinct, heavier isotopic composition (Fig. 5b). The range of sulfur isotope composition of rims observed in this study is similar to that observed in igneous sulfides and modern hydrothermal vents (Ono et al., 2007), and for the non-detrital component of Meteorite Bore Member pyrite, a hydrothermal origin is more likely. Delivery of secondary sulfide by a hydrothermal fluid is supported by enrichments (>0.5 wt.%) in minor elements including Co, Ni (Ohmoto and Goldhaber, 1997) and As (Ballantyne and Moore, 1988). Elemental enrichments observed in rims but not cores suggest that the rims do not originate from local sulfide that was dissolved and reprecipitated, but rather from a fluid that was enriched in these minor elements, as well as dissolved sulfide, and that percolated through the sediments sometime after deposition of the primary pyrite. The pattern observed in this study is similar to that seen in the Marshall Sandstone of southeastern Michigan, where As-rich (>7 wt.% As) pyrite overgrowths have formed on As-poor framboidal pyrite, leading to As concentrations of up to 300 μg/L in local groundwater (Kolker and Nordstrom, 2001).

A low grade metamorphic event (~200–300 °C) affecting the Turee Creek Group between ca. 2215 and ca. 2145 Ma has been proposed on the basis of monazite and xenotime U–Pb geochronology and may relate to the Opthalmian Orogeny (Rasmussen et al., 2005). Hydrothermal fluid flow during such an event is a likely source for the sulfide overgrowths and recrystallization observed in Meteorite Bore pyrites and is consistent with the sulfur isotope and minor element compositions reported here for the rims of zoned grains.

Yamaguchi and Ohmoto (2006) reported pyrites from the ~2.45 Ga Matinenda Fm of the Huronian Supergroup with $\delta^{34}S$ between −9‰ and 5.5‰, low Ni/Co (<1), and core–rim zonation in As, Ni, and Co. These authors assigned a volcanic–hydrothermal origin to the Matinenda Fm pyrite overgrowths on the basis that volcanogenic–hydrothermal pyrite tends to have high Co and low Ni/Co (<1), whereas Ni is typically more abundant in magmatic (Hawley and Nichol, 1961) and syngenetic/diagenetic, sedimentary (Kimberley et al., 1980) pyrite. By contrast, Meteorite Bore Member pyrites that have both Ni and Co above detection limits ("Ni–Co-enriched") exhibit a larger range in Ni/Co, tending towards higher values (0.1–5.6, with an average of 1.5). Pyrite grains with Ni/Co < 0.87 have $\delta^{34}S$ from 0‰ to 6.5‰, whereas those with higher Ni/Co have $\delta^{34}S$ from −37‰ to 12.8‰ (Fig. 11). This suggests that some of the high Ni/Co observed in Meteorite Bore Member pyrites is related to low-temperature sedimentary, rather than igneous processes, whereas the low Ni/Co pyrites could have a volcanic–hydrothermal source. Five Ni–Co-enriched pyrite grains classified as detrital based on their rounded margins and petrographic associations have Ni/Co between 0.8 and 2 and $\delta^{34}S$ between 0.6‰ and 6.5‰, consistent with an Archean magmatic source. Yamaguchi and Ohmoto (2006) attribute As-enrichment in the Matinenda Fm pyrite overgrowths

to reductive dissolution of deep basinal Fe- and Mn-hydroxides, As mobilization and fluid migration during early diagenesis, an interpretation that is consistent with our observations in the Meteorite Bore Member.

The general pattern of high $\delta^{34}S$ in overgrowth rims relative to cores is the same across different samples, although characteristic rim compositions differ. In sample 4, a mudrock low in the sequence, average $\delta^{34}S$ of rims is approximately 4‰. Average $\delta^{34}S$ of rims in sample 6, a coarser grained and likely more permeable rock higher in the sequence, is approximately 7‰ (Fig. 8). This compositional difference could be due to different pulses of fluid, or to differential dissolution of authigenic sulfides and incorporation into later-stage pyrite. Sample 4 has the highest proportion of authigenic pyrite with low $\delta^{34}S$ values (<−20‰) indicative of microbial sulfate reduction. Partial dissolution and reprecipitation of this original low $\delta^{34}S$ pyrite could explain the lower characteristic values of later stage pyrite in this sample.

4.2. Metamorphism and sulfur diffusion

Rasmussen et al. (2005) estimate that the Meteorite Bore Member was subjected to low-grade regional metamorphism at 200–300 °C for 70 Myr. These temperatures are consistent with the coexistence of pyrite and arsenopyrite in sample 5 (Fig. 7c). The phase relations of pyrite, arsenopyrite (FeAsS), and loellingite ($FeAs_2$) are reviewed by Sharp et al. (1985), who show the upper temperature stability of pyrite + arsenopyrite at 500 °C for low pressures and $\text{Log}(fS_2) \approx -4$. This temperature limit is lower for reduced sulfur fugacity, would be <300 °C at $\text{Log}(fS_2) < -9$, and is buffered by the composition of arsenopyrite. However, arsenopyrite in the Meteorite Bore Member has not yet been analyzed by EPMA to allow quantitative application of the arsenopyrite geothermometer.

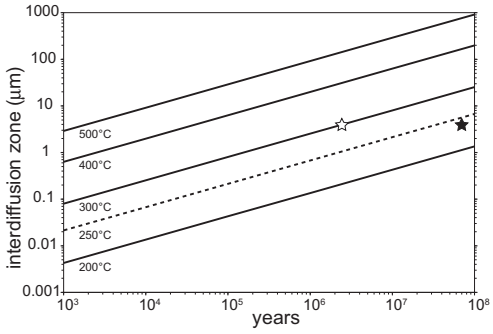

Fig. 12. Predicted width of the interdiffusion zone between isotopically distinct zones of pyrite, based on experimental determination of the rate of sulfur self-diffusion in pyrite (Watson et al., 2009). Figure modified from Fig. 9, Watson et al. (2009). Interdiffusion zone is defined as the distance interval encompassing 90% of the concentration difference between the two isotopically distinct zones. Filled star corresponds to a scenario in which a 4 μm interdiffusion zone is produced by a 70 Myr metamorphic event, indicating a maximum constant annealing temperature of ~240 °C. Open star indicates that constant exposure to a temperature of 300 °C for >2.5 Ma should produce an interdiffusion zone >4 μm. The measured gradient in Fig. 5a is less than 4 μm, indicating that these temperatures are upper limits.

Another way to constrain the temperature-time relations of these rocks involves the consideration of sulfur diffusion in pyrite. Small-spot sulfur isotope analyses in grains with visible core–rim zonation revealed isotopic gradients as large as 30‰ over a distance of less than 4 μm (Fig. 5a). Sharper gradients may exist, but are not resolved with a beam size of 3 μm. To our knowledge, these are the first high precision analyses of sulfur isotope ratios with a 3 μm spot and the sharpest sulfur isotope gradients yet observed in natural samples. If these gradients predate metamorphism, then consideration of rates of exchange across such gradients can provide useful constraints on thermal history.

Recent laboratory experiments have calibrated the temperature dependence of self-diffusion of sulfur in pyrite that allows for the modeling of isothermal interdiffusion:

$$D_S = 1.75 * 10^{-14} e^{(-132{,}100/RT)} \quad (2)$$

where R is the gas constant, and T is absolute temperature (Watson et al., 2009). Fig. 12 [modified from Fig. 9, Watson et al. (2009)] shows the predicted width of the interdiffusion zone between two isotopically distinct zones of pyrite assuming one-dimensional diffusion perpendicular to the contact as a function of time for constant temperature events of 200–500 °C. The interdiffusion zone is defined as the distance interval encompassing 90% of the concentration difference between the two isotopically distinct zones (Watson et al., 2009), which would be clearly resolvable in the zoned Meteorite Bore Member pyrites discussed here given the analytical precision of the 3 μm spot analyses. Modal scenarios represent the solutions to the following equation, modified from Watson et al. (2009, Eq. (4)):

$$\delta^{34}S(x,t) = \delta^{34}S_{\text{rim}} + \left(\frac{\delta^{34}S_{\text{core}} - \delta^{34}S_{\text{rim}}}{2}\right)\left(1 - erf\left(\frac{x}{2\sqrt{D_S t}}\right)\right) \quad (3)$$

where x is the distance in μm from the core–rim boundary, D_S is the diffusion coefficient of sulfur the at the temperature in question, and t is time. The assumption of 1-dimensional diffusive exchange vs. a 3-D model is justified by the sharp gradients shown in Fig. 5.

Our observations provide an upper constraint of 4 μm for the width of the interdiffusion zone in grain 29 from sample 6, and the interdiffusion zone may be significantly smaller (Fig. 5a). Furthermore, this calculation assumes an initial step profile; if there was any mixing across this boundary before metamorphism, then the constraints on temperature and time become more restrictive. These observations, together with results of calculations shown in Fig. 12, provide constraints on the temperature-time history for the Meteorite Bore Member. For the end-member case of a 70 Myr metamorphic event (Rasmussen et al., 2005), a 4 μm interdiffusion zone is produced by a constant annealing temperature of ~240 °C (solid star in Fig. 12). Similarly, using the upper temperature estimate of 300 °C

(Rasmussen et al., 2005), the maximum possible annealing time at peak metamorphic temperature to preserve an interdiffusion zone <4 μm is ~2.5 Myr (open star in Fig. 12).

4.3. Western Australian records of Archean–Proterozoic sulfur cycle evolution

The continuous sequence of continental margin environments preserved in Western Australia represents one of the best records of Earth system behavior during the Archean–Proterozoic transition (Barley et al., 2005). Sulfur isotope records from the 2.78 to 2.40 Ga Mt Bruce Supergroup (Nelson et al., 1999) have been critical to the development of the model of global sulfur cycle evolution and atmospheric oxygenation, and we briefly review them below. These previous records come from the oldest and intermediate subunits, the Fortescue and Hamersley Groups, and the present study is the first to present sulfur isotope data from the Turee Creek Group, the youngest subunit of the Mount Bruce Supergroup.

The initial report of the collapse of S-MIF at ~2.45 Ga by Farquhar et al. (2000) relied partly upon sulfur isotope data from the Fortescue and Hamersley Groups. Ono et al. (2003) presented a detailed study focusing on the Hamersley Basin, expanding the known range of variability in $\Delta^{33}S$ with values from −1.9‰ to 6.9‰ in the ~2.5 Ga Mount McRae Shale, −0.1‰ to 8.1‰ in the ~2.7 Ga Jeerinah Fm, and −2.5‰ to −1.1‰ in the ~2.6 Ga Carawine Dolomite. The relatively large range in $\delta^{34}S$ from the latter unit suggested an expansion in mass-dependent fractionation due to microbial sulfate reduction on the Carawine platform. The positive correlation between $\delta^{34}S$ and $\Delta^{33}S$ in shales of the Mount McRae and Jeerinah Fm was attributed to mixing of two sources of pyrite sulfur: (1) that derived from microbial sulfate reduction, characterized by low and variable $\delta^{34}S$ together with negative $\Delta^{33}S$ and (2) that derived from elemental sulfur, characterized by large, positive $\Delta^{33}S$ (Ono et al., 2003).

Earlier bulk data from the ~2.47 Ga Dales Gorge Member of the Brockman Iron Fm (Farquhar et al., 2000) were supported by in situ SIMS analyses of an individual pyrite microband yielding a range of −6.1 to −0.8 in $\delta^{34}S$ and −1.7‰ to 0‰ in $\Delta^{33}S$. Partridge et al. (2008) focused on the relationship of sulfur isotope composition to pyrite morphology and paragenesis, presenting data from the ~2.6 Ga Marra Mamba Iron Fm., the ~2.57 Ga Wittenoom Fm, the ~2.5 Ga Mount McRae Shale, and the ~2.48 Ga Dales Gorge and ~2.46 Whaleback Shale Members of the Brockman Iron Fm. This study distinguished pyrite nodules having isotopic compositions consistent with microbial sulfate reduction and fine-grained pyrite with compositions consistent with reduction of elemental sulfur in the Marra Mamba Iron Fm. Isotopic distinctions between pyrite morphotypes were less clear in the Wittenoom Fm, an observation the authors attributed to a shallower, perhaps more oxygenated depositional environment and multi-stage sulfur cycling in sediments. In the early Paleoproterozoic Brockman Iron Fm, the small range in $\delta^{34}S$ in the deeper water Dales Gorge Member was interpreted to represent the dominant influence of hydrothermal processes, whereas the highly positive $\delta^{34}S$ values in the shallower Whaleback Shale Member appear to record vigorous microbial sulfate reduction and Rayleigh fractionation in a more oxidized environment (Partridge et al., 2008).

4.4. Global correlation

Early Proterozoic glacial deposits in North America, South Africa, and Western Australia are bounded above and below by similarly age-constrained units. In North America, the maximum age of the glacials is constrained by the ca. 2450 Ma Copper Cliff Rhyolite (Krogh et al., 1984), in South Africa by the ca. 2432 Ma Penge and Griquatown BIFs (Trendall et al., 1990; Polteau et al., 2006), and in Western Australia, by the ca. 2450 Ma Woongarra Rhyolite (Barley et al., 1997) within the immediately conformably underlying Hamersley Basin. Minimum ages of the glacial units are provided by igneous rocks deposited during a 2220–2200 Ma global event of basaltic magmatism, representing breakout after the prolonged period of slowed mantle activity in the preceding 200–250 Ma (Condie et al., 2009). Thick flood basalt sequences of this age are recorded from Western Australia (2209 ± 15 Ma Cheela Springs Basalt; Martin et al., 1998) and South Africa (2222 ± 12 Ma Hekpoort and Ongeluk lavas; Cornell et al., 1996; Dorland, 2004). Equivalent intrusive rocks from North America include the extensive 2219 ± 3 to 2210 ± 3 Ma Nipissing diabase intrusions (Corfu and Andrews, 1986; Noble and Lightfoot, 1992) and Seneterre dykes (2216 + 8/−4 Ma; in Buchan et al., 1996), as also recorded in India (French and Heaman, 2010), and in China (2199 ± 11 Ma gneisses and 2193 ± 15 Ma gabbros; Zhao et al., 2008; Wang et al., 2010).

The Huronian Supergroup of Canada is the best studied of the Paleoproterozoic glacial successions so far identified. The three diamictite-bearing units of the supergroup include (from oldest to youngest) the Ramsay Lake, Bruce and Gowganda Formations (Young, 1981a,b, 2002). The Meteorite Bore Member may share a relative stratigraphic affinity with the lower glacial units of the Huronian Supergroup in the Ramsay Lake and Bruce Formations, rather than the Gowganda Fm as previously proposed (Martin, 1999). This interpretation is supported by the $\Delta^{33}S$ data from this study, which are comparable to those from the Pecors Fm, deposited between the first two glacial units in the Huronian Supergroup (Papineau et al., 2007) (Fig. 14).

In the Transvaal Basin of South Africa, two diamictite units have been identified in the Duitschland Fm (one at the base and one within the upper 200 m), and one in the upper Timeball Hill Fm (Bekker et al., 2001). S-MIF disappears, and the range of $\delta^{34}S$ expands, somewhere within a ~300 m interval of the upper Duitschland Fm above a prominent sequence boundary and between the lower two of the three Transvaal diamictites (Guo et al., 2009). Expansion in $\delta^{34}S$ in the upper Duitschland Fm is observed primarily as highly positive values in carbonate associated sulfate (Guo et al., 2009). Pyrites in the Rooihoogte Fm have $\delta^{34}S < -20‰$, and this unit in the southwest

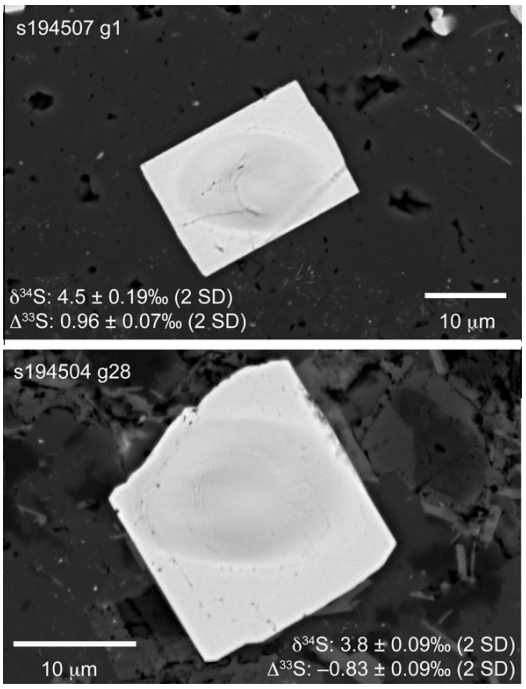

Fig. 13. Backscattered electron images of pyrites exhibiting the highest and lowest $\Delta^{33}S$ values in this study measured on grains that unambiguously grew in place. Ion microprobe pits from the March 23–27, 2010 analytical session at WiscSIMS are visible.

Transvaal Basin is time equivalent to the Duitschland Fm in the northeast (Bekker et al., 2004). On this basis we conclude that the Meteorite Bore Member correlates temporally with the lower part of the upper Duitschland Fm, during which the transition from mass-independent to mass-dependent sulfur isotope fractionation must have occurred (Guo et al., 2009).

4.5. Implications for atmospheric oxygenation

The rarity of detrital pyrite in sedimentary rocks younger than 2.2 Ga has been explained by the instability of pyrite under oxidizing conditions (Holland, 1984; Rasmussen and Buick, 1999). The presence of detrital pyrite in rocks older than 2.2 Ga has been used to provide an upper limit on atmospheric oxygen of about 0.01 PAL for this time (Buick, 2008; Frimmel, 2005). However, rare occurrences of detrital pyrite in sediments deposited in cold environments where chemical weathering rates are suppressed (Khim and Yoon, 2003) suggest that individual occurrences of detrital pyrite may provide an ambiguous constraint on atmospheric oxygen levels.

No rounded pyrite grains were identified in the glacial mudstone sample 4, from near the base of the succession studied herein, and the low $\delta^{34}S$ values in this sample support pyrite formation via microbial sulfate reduction. The range of $\Delta^{33}S$ in this sample is $-0.83‰$ to $0.68‰$, comparable to, but larger than the range reported for the Pecors Fm ($-0.07‰$ to $0.88‰$) in the Huronian Supergroup (Papineau et al., 2007). When the small, euhedral grains from the BIF units that bound the Meteorite Bore Member are included, the total range of $\Delta^{33}S$ for the sequence expands to $-0.83‰$ to $0.96‰$ (Figs. 13 and 14b). We argue that this is a conservative range of $\Delta^{33}S$ for authigenic pyrite from the Meteorite Bore Member and excludes any detrital component.

The $90‰$ range in $\delta^{34}S$ of Meteorite Bore Member pyrite is significantly larger than any observed prior to the Neoproterozoic (Fig. 14a) and implies a seawater sulfate concentration above 200 μM by the time of deposition (Habicht et al., 2002). The Archean–Proterozoic increase in seawater sulfate is thought to have been driven by increased oxidative weathering of sulfides on the continents and must have occurred before deposition of the 2.316 ± 0.007 Ga Timeball Hill Fm (Hannah et al., 2004) with $\delta^{34}S < -30‰$ and $-0.2‰ < \Delta^{33}S < 0.4‰$ (Bekker et al., 2004).

A series of studies reporting geochemical analyses of the portion of the Archean Biosphere Drilling Project (ABDP)-9 core intersecting the ~2.5 Ga Mount McRae Shale have shown enrichments in redox sensitive elements (Anbar et al., 2007) and shifts in the isotopic compositions of sedimentary sulfur (Kaufman et al., 2007) and nitrogen (Garvin et al., 2009), all pointing to the onset of oxidative processes well before pervasive atmospheric oxygenation and the disappearance of S-MIF. Iron speciation data from the same interval of the ABDP-9 core show evidence for euxinia, attributed to enhanced delivery of organic carbon and dissolved sulfate to the anoxic deep ocean (Reinhard et al., 2009). Extrapolation of rates determined in the laboratory suggests that the kinetics of pyrite dissolution under atmospheric oxygen concentrations between 10^{-8} and 10^{-5} PAL permit the delivery of a significant quantity of dissolved sulfate to the ocean from continental weathering on sub-million year timescales (Reinhard et al., 2009). The range of $\delta^{34}S$ observed in the Mount McRae shale ($-6.1‰$ to $11.7‰$) is significantly lower than that observed in the Meteorite Bore Member ($-45.5‰$ to $46.4‰$), pointing to a further increase in seawater sulfate between the deposition of the two units.

Biogeochemical models simulating the conditions that gave rise to the GOE seek to clarify the complex relations between seawater sulfate, atmospheric methane and oxygen, hydrogen escape, and global temperature. Catling et al. (2001) described the slow, but irreversible oxidation of Earth's surface that would have occurred as the result of elevated hydrogen escape during an Archean methane greenhouse. Zahnle et al. (2006) demonstrated how the initial collapse of the methane greenhouse would have curtailed the efficient reduction of sulfur-bearing, volcanic gases to elemental sulfur, an essential barrier against dilution or loss of the S-MIF signal due to oceanic mixing (Pavlov and Kasting, 2002). Claire et al. (2006) advanced a model supporting the hypothesis that the timing of the GOE was controlled primarily by decreasing fluxes of reducing volatiles and generating three "Snowball Earth" events between 2.4 and 2.3 Ga due to biospheric feedbacks between global temperature, oxygen, methane and carbon dioxide. Catling et al. (2007) explored the critical relationship between seawater sulfate and atmospheric methane

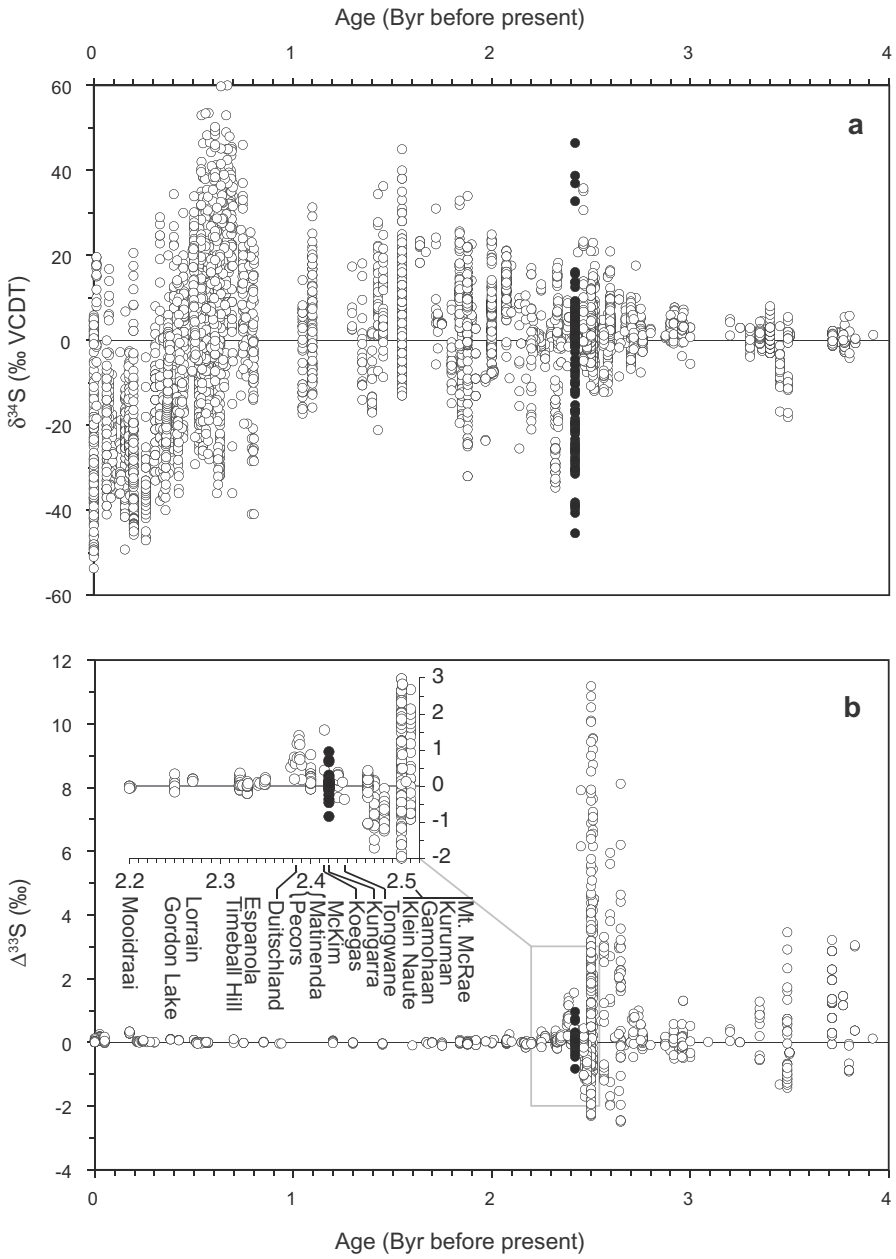

Fig. 14. Compilations of $\delta^{34}S$ (a) and $\Delta^{33}S$ values (b) including previously published data (open circles) and WiscSIMS data from this study (filled circles). Only sulfide data are shown in (a), whereas sulfide and sulfate data are shown in (b). Enlargement in (b) shows the critical time interval for atmospheric oxygenation. Formation names for associated data are indicated in (b). $\Delta^{33}S$ data shown from this study exclude pyrite of detrital or ambiguous origin. Figures are adapted from previously published compilations (Farquhar et al., 2007b; Canfield and Farquhar, 2009; Domagal-Goldman et al., 2008) and incorporate additional data (Papineau et al., 2007; Partridge et al., 2008; Ueno et al., 2008; Guo et al., 2009; Ono et al., 2009; Williford et al., 2009; Wu et al., 2010).

concentrations as mediated by the anaerobic oxidation of methane in marine sediments by consortia of methanotrophic archaea and sulfate reducing bacteria. In an anoxic Archean world, low seawater sulfate concentrations would have limited this metabolism and permitted a large flux of methane from the oceans to the atmosphere. As seawater sulfate concentrations increased, anaerobic oxidation of methane in sediments facilitated a more rapid rise in oxygen amid the collapse of the methane greenhouse (Catling et al., 2007).

Along with dissolved sulfate, trace elements in seawater likely played an important role in changing the magnitude of atmospheric oxygen sources and sinks during the Archean–Proterozoic transition. Since phosphorous is an important rate-limiting nutrient for oxygenic photosynthesis (Holland, 1984), an increased delivery of bioavailable phosphate to the oceans as a result of intense chemical weathering associated with high tectonic activity followed by global glaciation in the earliest Paleoproterozoic may have led to an increased source of atmospheric oxygen (Papineau, 2010). However, high phosphorous concentrations in Archean and Paleoproterozoic iron formations relative to their younger counterparts suggest that other micronutrients may have been more limiting (Planavsky et al., 2010). Because several enzymes critical to microbial methanogenesis use Ni cofactors, a decline in Ni/Fe ratios in iron formations between 2.7 and 2.5 Ga has been dubbed a "nickel famine" and implicated in the collapse of the Archean methane greenhouse (Konhauser et al., 2009).

Although the disappearance of S-MIF and appearance of large mass dependent sulfur isotope fractionations have been documented in the Huronian (Papineau et al., 2007) and Transvaal (Guo et al., 2009) supergroups, the data presented here represent the first observations of significant S-MIF together with large, mass-dependent sulfur isotope fractionations. This lends important empirical insight into the temporal ordering of events generated in the biogeochemical models described above. Zahnle et al. (2006) speculated that the increasing pool of seawater sulfate due to the progressive oxidation of the atmosphere–ocean–crust system driven by hydrogen escape (Catling et al., 2001) was responsible for the reduction of atmospheric methane below 10 ppmv, shutting down the production of atmospheric S_8 and thus the preservation of S-MIF. Our data clearly support this order of events and further highlight the role that microbial sulfate reduction played in establishing the conditions necessary for the oxygenation of Earth's atmosphere.

5. CONCLUSIONS

In situ analysis of authigenic pyrites from Paleoproterozoic glaciogenic rocks of the Meteorite Bore Member of the Turee Creek Group, Western Australia show a small, but significant range of S-MIF ($\Delta^{33}S$ from to $-0.83‰$ to $0.96 \pm 0.09‰$) and a $90‰$ range of $\delta^{34}S$ ($-45.5‰$ to $46.4‰$) that is larger than any observed in rocks older than 700 Ma. Meteorite Bore Member diamictites contain detrital pyrite with a range of $\Delta^{33}S$ ($-3.57‰$ to $11.73‰$) larger than any previously reported. In light of published atmospheric models, these data suggest that the Meteorite Bore Member was deposited while atmospheric oxygen was in transition, perhaps between 10^{-8} and 10^{-2} PAL (Pavlov and Kasting, 2002; Reinhard et al., 2009). This strengthens the argument that diamictites of the Meteorite Bore Member can be temporally correlated with the lower glacial units of the Huronian Supergroup and the lower part of the Upper Duitschland Fm in the Transvaal Supergroup. Clearly, the initial Paleoproterozoic glaciations were associated with rapid biogeochemical changes in Earth's atmosphere, oceans, and upper crust.

Multiple generations of pyrite are present in rocks of the Meteorite Bore Member. Pyrite grains with low $\delta^{34}S$ ($<-20‰$) indicative of microbial sulfate reduction are in some cases overgrown by euhedral rims that have higher positive values of $\delta^{34}S$ (4–7‰) and higher concentrations of As, Ni, and Co, suggesting a hydrothermal source. Extremely sharp intra-grain gradients observed in situ with small-spot sulfur isotope analyses across core–rim boundaries ($30‰$ in $\delta^{34}S$ over <4 μm) indicate that pyrite cores preserve original sulfur isotope signatures. Calculations of sulfur diffusion distances set an upper temperature limit of 240 °C for a 70 Myr metamorphic event (Rasmussen et al., 2005) in order to preserve the isotopic gradients as observed. Furthermore, it is possible that earlier hydrothermal events also affected these gradients in $\delta^{34}S$, in which case any metamorphism must have been less intense (lower temperature or shorter time) in order to preserve the measured profile (Figs. 5 and 11).

The extreme sulfur isotopic variability at the micrometer scale in the Meteorite Bore Member pyrites revealed by SIMS would be largely masked by "bulk" techniques, leading to dramatically different conclusions. This underscores the critical importance of in situ isotopic microanalysis in petrographic context as a tool in future efforts to characterize the behavior of planetary systems in time and space.

ACKNOWLEDGEMENTS

We thank Noriko Kita and Jim Kern for assistance and training with the ion microprobe, Brian Hess for sample preparation, John Fournelle for assistance in the operation of the SEM and electron microprobe, Jason Huberty for assistance with the SEM, and Clark Johnson, Brian Beard, and Andy Czaja for helpful discussions. Funding was provided by the NASA Astrobiology Institute. The WiscSIMS Lab is partially funded by NSF-EAR (0319230, 0516725, 0744079). We thank Associate Editor James Farquhar and reviewers David Johnston, Shuhei Ono, and Dominic Papineau for their constructive comments that improved the quality of this manuscript.

APPENDIX A. SUPPLEMENTARY DATA

Supplementary data associated with this article can be found, in the online version, at doi:10.1016/j.gca.2011.07.010.

REFERENCES

Anbar A. D., Duan Y., Lyons T. W., Arnold G. L., Kendall B., Creaser R. A., Kaufman A. J., Gordon G. W., Scott C., Garvin J. and Buick R. (2007) A whiff of oxygen before the Great Oxidation Event? *Science* **317**, 1903–1906.

Ballantyne J. M. and Moore J. N. (1988) Arsenic geochemistry in geothermal systems. *Geochim. Cosmochim. Acta* **52**, 475–483.

Barley M. E., Bekker A. and Krapez B. (2005) Late Archean to Early Paleoproterozoic global tectonics, environmental change and the rise of atmospheric oxygen. *Earth Planet. Sci. Lett.* **238**, 156–171.

Barley M. E., Pickard A. L. and Sylvester P. J. (1997) Emplacement of a large igneous province as a possible cause of banded iron formation 2.45 billion years ago. *Nature* **385**, 55–58.

Barrie C., Taylor C. and Ames D. (2005) Geology and metal contents of the ruttan volcanogenic massive sulfide deposit, northern manitoba, canada. *Miner. Deposita* **39**, 795–812.

Bekker A., Holland H. D., Wang P. L., Rumble D., Stein H. J., Hannah J. L., Coetzee L. L. and Beukes N. J. (2004) Dating the rise of atmospheric oxygen. *Nature* **427**, 117–120.

Bekker A., Kaufman A. J., Karhu J. A., Beukes N. J., Swart Q. D., Coetzee L. L. and Eriksson K. A. (2001) Chemostratigraphy of the paleoproterozoic Duitschland Formation, South Africa: implications for coupled climate change and carbon cycling. *Am. J. Sci.* **301**, 261–285.

Blake T. S. and Barley M. E. (1992) Tectonic evolution of the Late Archean to Early Proterozoic Mount Bruce Megasequence Set, Western Australia. *Tectonics* **11**, 1415–1425.

Buchan K. L., Halls H. C. and Mortensen J. K. (1996) Paleomagnetism, U–Pb geochronology, and geochemistry of Marathon dykes, Superior province, and comparison with the Fort Frances swarm. *Can. J. Earth Sci.* **33**, 1583–1595.

Buick R. (2008) When did oxygenic photosynthesis evolve? *Philos. Trans. R. Soc. B. Biol. Sci.* **363**, 2731–2743.

Cameron E. M. (1982) Sulfate and sulfate reduction in early Precambrian oceans. *Nature* **296**, 145–148.

Cameron E. M. and Hattori K. (1987) Archean sulfur cycle – evidence from sulfate minerals and isotopically fractionated sulphides in Superior Province, Canada. *Chem. Geol.* **65**, 341–358.

Canfield D. E. and Farquhar J. (2009) Animal evolution, bioturbation, and the sulfate concentration of the oceans. *Proc. Natl. Acad. Sci. USA* **106**, 8123–8127.

Catling D. C. and Claire M. W. (2005) How Earth's atmosphere evolved to an oxic state: a status report. *Earth Planet. Sci. Lett.* **237**, 1–20.

Catling D. C., Claire M. W. and Zahnle K. J. (2007) Anaerobic methanotrophy and the rise of atmospheric oxygen. *Philos. Trans. R. Soc. A. Math. Phys. Eng. Sci.* **365**, 1867–1888.

Catling D. C., Zahnle K. J. and McKay C. P. (2001) Biogenic methane, hydrogen escape, and the irreversible oxidation of early Earth. *Science* **293**, 839–843.

Claire M. W., Catling D. C. and Zahnle K. J. (2006) Biogeochemical modelling of the rise in atmospheric oxygen. *Geobiology* **4**, 239–269.

Condie K. C., O'Neill C. and Aster R. C. (2009) Evidence and implications for a widespread magmatic shutdown for 250 My on Earth. *Earth Planet. Sci. Lett.* **282**, 294–298.

Corfu F. and Andrews A. J. (1986) A U–Pb age for mineralized Nipissing Diabase, Gowganda, Ontario. *Can. J. Earth Sci.* **23**, 107–109.

Cornell D. H., Schutte S. S. and Eglington B. L. (1996) The Ongeluk basaltic andesite formation in Griqualand West, South Africa: Submarine alteration in a 2222 Ma Proterozoic sea. *Precambrian Res.* **79**, 101–123.

Crowe D. E. and Vaughan R. G. (1996) Characterization and use of isotopically homogeneous standards for in situ laser microprobe analysis of S-34/S-32 ratios. *Am. Mineral.* **81**, 187–193.

Ding T., Valkiers S., Kipphardt H., De Bievre P., Taylor P. D. P., Gonfiantini R. and Krouse R. (2001) Calibrated sulfur isotope abundance ratios of three IAEA sulfur isotope reference materials and V-CDT with a reassessment of the atomic weight of sulfur. *Geochim. Cosmochim. Acta* **65**, 2433–2437.

Domagal-Goldman S. D., Kasting J. F., Johnston D. T. and Farquhar J. (2008) Organic haze, glaciations and multiple sulfur isotopes in the Mid-Archean Era. *Earth Planet. Sci. Lett.* **269**, 29–40.

Donovan J. J. (2009) Probe for EPMA - User's Guide and Reference Manual, Advanced Microbeam Inc. In: (eds. J.J. Donovan, D. Kremser, J. Fournelle). 355p.

Dorland H. C. (2004) *Provenance Ages and Timing of Sedimentation of Selected Neoarchean and Paleoproterozoic Successions of the Kaapvaal craton*. Rand Afrikaans University, Johannesburg, South Africa, p. 326.

Evans D. A., Beukes N. J. and Kirschvink J. L. (1997) Low-latitude glaciation in the Palaeoproterozoic era. *Nature* **386**, 262–266.

Eyles N. (1993) Earth's glacial record and its tectonic setting. *Earth Sci. Rev.* **35**, 1–248.

Farquhar J., Bao H. M. and Thiemens M. (2000) Atmospheric influence of Earth's earliest sulfur cycle. *Science* **289**, 756–758.

Farquhar J., Johnston D. T. and Wing B. A. (2007a) Implications of conservation of mass effects on mass-dependent isotope fractionations: influence of network structure on sulfur isotope phase space of dissimilatory sulfate reduction. *Geochim. Cosmochim. Acta* **71**, 5862–5875.

Farquhar J., Peters M., Johnston D. T., Strauss H., Master A., Wiechert U. and Kaufman A. J. (2007b) Isotopic evidence for mid-Archean anoxia. *Geochim. Cosmochim. Acta* **71**, A269.

Farquhar J., Savarino J., Airieau S. and Thiemens M. H. (2001) Observation of wavelength-sensitive mass-independent sulfur isotope effects during SO_2 photolysis: implications for the early atmosphere. *J. Geophys. Res. Planets* **106**, 32829–32839.

Fournelle J. H., Kim S. and Perepezko J. H. (2005) Monte Carlo simulation of NbK alpha secondary fluorescence in EPMA: comparison of PENELOPE simulations with experimental results. *Surf. Interface Anal.* **37**, 1012–1016.

French J. E. and Heaman L. M. (2010) Precise U–Pb dating of Paleoproterozoic mafic dyke swarms of the Dharwar craton, India: implications for the existence of the Neoarchean supercraton Sclavia. *Precambrian Res.* **183**, 416–441.

Frimmel H. E. (2005) Archaean atmospheric evolution: evidence from the Witwatersrand gold fields, South Africa. *Earth Sci. Rev.* **70**, 1–46.

Garvin J., Buick R., Anbar A. D., Arnold G. L. and Kaufman A. J. (2009) Isotopic evidence for an aerobic nitrogen cycle in the latest archean. *Science* **323**, 1045–1048.

Guo Q. J., Strauss H., Kaufman A. J., Schroder S., Gutzmer J., Wing B., Baker M. A., Bekker A., Jin Q. S., Kim S. T. and Farquhar J. (2009) Reconstructing Earth's surface oxidation across the Archean–Proterozoic transition. *Geology* **37**, 399–402.

Habicht K. S., Gade M., Thamdrup B., Berg P. and Canfield D. E. (2002) Calibration of sulfate levels in the Archean Ocean. *Science* **298**, 2372–2374.

Hannah J. L., Bekker A., Stein H. J., Markey R. J. and Holland H. D. (2004) Primitive Os and 2316 Ma age for marine shale: implications for Paleoproterozoic glacial events and the rise of atmospheric oxygen. *Earth Planet. Sci. Lett.* **225**, 43–52.

Hawley J. E. and Nichol I. (1961) Trace elements in pyrite, pyrrhotite and chalcopyrite of different ores. *Econ. Geol.* **56**, 467–487.

Heck P. R., Ushikubo T., Schmitz B., Kita N. T., Spicuzza M. J. and Valley J. W. (2010) A single asteroidal source for extraterrestrial Ordovician chromite grains from Sweden and China: high-precision oxygen three-isotope SIMS analysis. *Geochim. Cosmochim. Acta* **74**, 497–509.

Holland H. D. (1984) *The chemical evolution of the atmosphere and oceans*. Princeton University Press, Princeton, New Jersey.

Holland H. D. (1994) Early Proterozoic atmospheric change. In: *Early Life on Earth* (ed. S. Bengston). Nobel Symposium 84, 237–244.

Holland H. D. (2002) Volcanic gases, black smokers, and the Great Oxidation Event. *Geochim. Cosmochim. Acta* **66**, 3811–3826.

Hulston J. R. and Thode H. G. (1965) Variations in S^{33}, S^{34} and S^{36} contents of meteorites and their relation to chemical and nuclear effects. *J. Geophys. Res.* **70**, 3475–3484.

Kaufman A. J., Johnston D. T., Farquhar J., Masterson A. L., Lyons T. W., Bates S., Anbar A. D., Arnold G. L., Garvin J. and Buick R. (2007) Late Archean biospheric oxygenation and atmospheric evolution. *Science* **317**, 1900–1903.

Khim B. K. and Yoon H. I. (2003) Postglacial marine environmental changes in Maxwell Bay, King George Island, West Antarctica. *Polar. Res.* **22**, 341–353.

Kimberley M. M., Tanaka R. T. and Farr M. R. (1980) Composition of Middle Precambrian uraniferous conglomerate in the Elliot Lake–Agnew Lake area of Canada. *Precambrian Res.* **12**, 375–392.

Kirschvink J. L., Gaidos E. J., Bertani L. E., Beukes N. J., Gutzmer J., Maepa L. N. and Steinberger R. E. (2000) Paleoproterozoic snowball Earth: extreme climatic and geochemical global change and its biological consequences. *Proc. Natl. Acad. Sci. USA* **97**, 1400–1405.

Kita N. T., Nagahara H., Tachibana S., Tomomura S., Spicuzza M. J., Fournelle J. H. and Valley J. W. (2010) High precision SIMS oxygen three isotope study of chondrules in LL3 chondrites: role of ambient gas during chondrule formation. *Geochim. Cosmochim. Acta* **74**, 6610–6635.

Kita N. T., Ushikubo T., Fu B. and Valley J. W. (2009) High precision SIMS oxygen isotope analysis and the effect of sample topography. *Chem. Geol.* **264**, 43–57.

Kolker A., Nordstrom D. K. (2001) Occurrence and microdistribution of arsenic in pyrite. Proceedings of the USGS Arsenic Workshop. U.S. Geological Survey, Denver, p. 3.

Konhauser K. O., Pecoits E., Lalonde S. V., Papineau D., Nisbet E. G., Barley M. E., Arndt N. T., Zahnle K. and Kamber B. S. (2009) Oceanic nickel depletion and a methanogen famine before the Great Oxidation Event. *Nature* **458**, U750–U785.

Kozdon R., Kita N. T., Huberty J. M., Fournelle J. H., Johnson C. A. and Valley J. W. (2010) In situ sulfur isotope analysis of sulfide minerals by SIMS: precision and accuracy, with application to thermometry of similar to 3.5 Ga Pilbara cherts. *Chem. Geol.* **275**, 243–253.

Krogh T. E., Davis D. W., Corfu F. (1984) Precise U–Pb zircon and baddeleyite ages for the Sudbury area. In: *The Geology and Ore Deposits of the Sudbury Structure* (eds. E.G. Pye, A.J. Naldrett, P.E. Gilblin). Special Paper 1. Ontario Geological Survey, pp. 431–446.

Lyons J. R. (2009) Atmospherically-derived mass-independent sulfur isotope signatures, and incorporation into sediments. *Chem. Geol.* **267**, 164–174.

Machel H. G., Krouse H. R. and Sassen R. (1995) Products and distinguishing criteria of bacterial and thermochemical sulfate reduction. *Appl. Geochem.* **10**, 373–389.

Martin D. M. (1999) Depositional setting and implications of Paleoproterozoic glaciomarine sedimentation in the Hamersley Province, Western Australia. *Geol. Soc. Am. Bull.* **111**, 189–203.

Martin D. M., Li Z. X., Nemchin A. A. and Powell C. M. (1998) A pre-2.2 Ga age for giant hematite ores of the Hamersley province, Australia? *Econ. Geol. Bull. Soc. Econ. Geol.* **93**, 1084–1090.

Müller S. G., Krapez B., Barley M. E. and Fletcher I. R. (2005) Giant iron-ore deposits of the Hamersley province related to the breakup of Paleoproterozoic Australia: new insights from in situ SHRIMP dating of baddeleyite from mafic intrusions. *Geology* **33**, 577–580.

Nelson D. R., Trendall A. F. and Altermann W. (1999) Chronological correlations between the Pilbara and Kaapvaal cratons. *Precambrian Res.* **97**, 165–189.

Noble S. R. and Lightfoot P. C. (1992) U–Pb baddeleyite ages of the Kerns and Triangle Mountain intrusions, Nipissing Diabase, Ontario. *Can. J. Earth Sci.* **29**, 1424–1429.

Ohmoto H. and Goldhaber M. B. (1997) Sulfur and carbon isotopes. In *Geochemistry of Hydrothermal Ore Systems* (ed. H. L. Barnes). Wiley, New York, pp. 517–611.

Ono S., Eigenbrode J. L., Pavlov A. A., Kharecha P., Rumble D., Kasting J. F. and Freeman K. H. (2003) New insights into Archean sulfur cycle from mass-independent sulfur isotope records from the Hamersley Basin, Australia. *Earth Planet. Sci. Lett.* **213**, 15–30.

Ono S., Shanks W. C., Rouxel O. J. and Rumble D. (2007) S-33 constraints on the seawater sulfate contribution in modern seafloor hydrothermal vent sulfides. *Geochim. Cosmochim. Acta* **71**, 1170–1182.

Ono S. H., Beukes N. J. and Rumble D. (2009) Origin of two distinct multiple-sulfur isotope compositions of pyrite in the 2.5 Ga Klein Naute Formation, Griqualand West Basin, South Africa. *Precambrian Res.* **169**, 48–57.

Papineau D. (2010) Global biogeochemical changes at both ends of the proterozoic: insights from phosphorites. *Astrobiology* **10**, 165–181.

Papineau D., Mojzsis S. J., Coath C. D., Karhu J. A. and McKeegan K. D. (2005) Multiple sulfur isotopes of sulfides from sediments in the aftermath of Paleoproterozoic glaciations. *Geochim. Cosmochim. Acta* **69**, 5033–5060.

Papineau D., Mojzsis S. J. and Schmitt A. K. (2007) Multiple sulfur isotopes from Paleoproterozoic Huronian interglacial sediments and the rise of atmospheric oxygen. *Earth Planet. Sci. Lett.* **255**, 188–212.

Partridge M. A., Golding S. D., Baublys K. A. and Young E. (2008) Pyrite paragenesis and multiple sulfur isotope distribution in late Archean and early Paleoproterozoic Hamersley Basin sediments. *Earth Planet. Sci. Lett.* **272**, 41–49.

Pavlov A. A. and Kasting J. F. (2002) Mass-independent fractionation of sulfur isotopes in Archean sediments: strong evidence for an anoxic Archean atmosphere. *Astrobiology* **2**, 27–41.

Planavsky N. J., Rouxel O. J., Bekker A., Lalonde S. V., Konhauser K. O., Reinhard C. T. and Lyons T. W. (2010) The evolution of the marine phosphate reservoir. *Nature* **467**, 1088–1090.

Polteau S., Moore J. M. and Tsikos H. (2006) The geology and geochemistry of the Palaeoproterozoic Makganyene diamictite. *Precambrian Res.* **148**, 257–274.

Rasmussen B. and Buick R. (1999) Redox state of the Archean atmosphere: evidence from detrital heavy minerals in ca. 3250–2750 Ma sandstones from the Pilbara Craton, Australia. *Geology* **27**, 115–118.

Rasmussen B., Fletcher I. R. and Sheppard S. (2005) Isotopic dating of the migration of a low-grade metamorphic front during orogenesis. *Geology* **33**, 773–776.

Reinhard C. T., Raiswell R., Scott C., Anbar A. D. and Lyons T. W. (2009) A late archean sulfidic sea stimulated by early oxidative weathering of the continents. *Science* **326**, 713–716.

Sharp Z. D., Essene E. J. and Kelly W. C. (1985) A re-examination of the arsenopyrite geothermometer: pressure considerations and applications to natural assemblages. *Can. Mineral.* **23**, 517–534.

Shen Y. A., Buick R. and Canfield D. E. (2001) Isotopic evidence for microbial sulphate reduction in the early Archaean era. *Nature* **410**, 77–81.

Smith R. E., Perdrix J. L. and Parks T. C. (1982) Burial metamorphism in the Hamersley Basin, Western Australia. *J. Petrol.* **23**, 75–102.

Summons R. E., Bradley A. S., Jahnke L. L. and Waldbauer J. R. (2006) Steroids, triterpenoids and molecular oxygen. *Philos. Trans. R. Soc. B. Biol. Sci.* **361**, 951–968.

Takehara M., Komure M., Kiyokawa S., Horie K., Yokohama K. (2010) Detrital zircon SHRIMP U–Pb age of the 2.3 Ga diamictites of the Meteorite Bore Member in the South Pilbara, Western Australia. In: (eds. I.M. Tyler, C.M. Knox-Robinson), Fifth International Archean Symposium Abstracts: Geological Survey of Western Australia, Record 2010/18, pp. 223–224.

Trendall A. F. (1976) Striated and faceted boulders from the Turee Creek Formation-Evidence for a possible Huronian glaciation on the Australian continent. *Geological Survey of Western Australia Annual Report 1975*, 88–92.

Trendall A. F. (1981) The Lower Proterozoic Meteorite Bore Member, Hamersley Basin, Western Australia. In *Earth's pre-Pleistocene Glacial Record* (eds. M. J. Hambrey and W. B. Harland). Cambridge University Press, Cambridge, pp. 555–557.

Trendall A. F., Compston I. S., Williams R. A., Armstrong N. T., Arndt N. T., McNaughton N. J., Nelson D. R., Barley M. E., Beukes J. K., De Laeter J. R., Retief E. A., Thorne A. M. (1990) Precise zircon U–Pb chronological comparison of the volacno-sedimentary sequences of teh Kaapvaal and Pilbara Cratons between about 3.1 and 2.4 Ga. In: *Proceedings of the Third International Archean Symposium* (eds. J.E. Glover, S.E. Ho). Perth, Geoconferences (W.A.), Inc., Perth, pp. 81–83.

Ueno Y., Ono S., Rumble D. and Maruyama S. (2008) Quadruple sulfur isotope analysis of ca. 3.5 Ga Dresser Formation: new evidence for microbial sulfate reduction in the early Archean. *Geochim. Cosmochim. Acta* **72**, 5675–5691.

Valley J. W., Kita N. T. (2009) *In situ* oxygen isotope geochemistry by ion microprobe. In: *MAC Short Course: Secondary Ion Mass Spectrometry in the Earth Sciences* (ed. M. Fayek), pp. 19–63.

Van Kranendonk M. J. (2010) Three and a Half Billion Years of Life on Earth: a Transect Back Into Deep Time. Geological Survey of Western Australia Record 2010/21. Geological Survey of Western Australia, East Perth.

Waldbauer J. R., Sherman L. S., Sumner D. Y. and Summons R. E. (2009) Late Archean molecular fossils from the Transvaal Supergroup record the antiquity of microbial diversity and aerobiosis. *Precambrian Res.* **169**, 28–47.

Wang Z. H., Wilde S. A. and Wan J. L. (2010) Tectonic setting and significance of 2.3–2.1 Ga magmatic events in the Trans-North China Orogen: New constraints from the Yanmenguan mafic–ultramafic intrusion in the Hengshan–Wutai–Fuping area. *Precambrian Res.* **178**, 27–42.

Watson E. B., Cherniak D. J. and Frank E. A. (2009) Retention of biosignatures and mass-independent fractionations in pyrite: self-diffusion of sulfur. *Geochim. Cosmochim. Acta* **73**, 4792–4802.

Williford K. H., Foriel J., Ward P. D. and Steig E. J. (2009) Major perturbation in sulfur cycling at the Triassic–Jurassic boundary. *Geology* **37**, 835–838.

Wu N. P., Farquhar J., Strauss H., Kim S. T. and Canfield D. E. (2010) Evaluating the S-isotope fractionation associated with Phanerozoic pyrite burial. *Geochim. Cosmochim. Acta* **74**, 2053–2071.

Yamaguchi K. E. and Ohmoto H. (2006) Evidence from sulfur isotope and trace elements in pyrites for their multiple post-depositional processes in uranium ores at the Stanleigh Mine, Elliot Lake, Ontario, Canada. In *Evolution of Earth's Early Atmosphere, Hydrosphere, and Biosphere-Constraints from Ore Deposits: Geological Society of America Memoir 198* (eds. S. E. Kesler and H. Ohmoto). Geological Society of America, Denver, pp. 143–156.

Young G. M. (1981a) Diamictites of the Early Proterozoic Ramsay Lake and Bruce Formations, north shore of Lake Huron, Ontario, Canada. In *Earth's pre-Pleistocene Glacial Record* (eds. M. J. Hambrey and W. B. Harland). Cambridge University Press, Cambridge, pp. 813–816.

Young G. M. (1981b) The Early Proterozoic Gowganda Formation, Ontario, Canada. In *Earth's pre-Pleistocene Glacial Record* (eds. M. J. Hambrey and W. B. Harland). Cambridge University Press, Cambridge, pp. 807–812.

Young G. M. (2002) Stratigraphic and tectonic settings of Proterozoic glaciogenic rocks and banded iron-formations: relevance to the snowball Earth debate. *J. Afr. Earth Sc.* **35**, 451–466.

Zahnle K., Claire M. and Catling D. (2006) The loss of mass-independent fractionation in sulfur due to a Palaeoproterozoic collapse of atmospheric methane. *Geobiology* **4**, 271–283.

Zhao G. C., Wilde S. A., Sun M., Li S. Z., Li X. P. and Zhang J. (2008) SHRIMP U–Pb zircon ages of granitoid rocks in the Luliang Complex: implications for the accretion and evolution of the Trans-North China Orogen. *Precambrian Res.* **160**, 213–226.

Associate editor: James Farquhar